Single and Dual-Parameter Fiber Bragg Grating Sensors Embedded in Metallic Structures

by

Philippe Meszaros

A thesis
presented to the University of Waterloo
in fulfillment of the
thesis requirement for the degree of
Master of Applied Science
in
Mechanical Engineering

Waterloo, Ontario, Canada, 2017

I hereby declare that I am the sole author of this thesis. This is a true copy of the thesis, including any required final revisions, as accepted by my examiners.

Abstract

Fiber Bragg Gratings (FBGs) are optical fiber sensors that can be used to measure both strain and temperature. Due to their robustness, FBG sensors can be more easily embedded into materials than traditional electronic sensors. In this thesis a procedure to embed FBG sensors into metallic structures was developed. This embedding procedure used traditional machining, along with silver nanoparticle paste as an adhesive to embed FBGs into metallic parts. This new embedding procedure requires no specialized equipment and allows any metallic part to be retrofitted with embedded sensors.

Three main analytical models were developed in this thesis. The first analytical model was used to describe how strain is transferred from the host material to the embedded fiber. The second model described the dependence of the Bragg wavelength of an FBG to temperature and strain. The third model was used to predict reflection spectra of FBGs depending on strain distribution along the length of fibers. These analytical models along with finite element analysis were used to design both single and dual-parameter embedded FBG sensors.

A total of 22 single-parameter sensors built using silver nanoparticle embedding were subject to tensile testing a repeatability testing. The embedded sensors behaved linearly and performed well up to 350°C. The single-parameter sensors recorded strain up to the mean failure strain of 1.6% at 25°C and 0.93% at 350°C in the tensile tests. Although both the tensile tests and the repeatability tests showed the promise of silver nanoparticle embedded FBGs, significant signal noise during the testing caused some uncertainty about the sensitivity of the samples.

A single dual-parameter sensor prototype was also built using silver nanoparticle embedding. This sample was subject to a tensile test and a temperature test to examine it's sensitivity. The average error between the sensitivities recorded during the dual-parameter tests and the sensitivities predicted by the analytical models developed in this thesis was 2.9%.

The designs for the single and dual-parameter sensors show potential for use in high temperature aerospace and automotive applications. Better characterization of embedded FBG sensors produced using silver nanoparticle embedding is warranted.

Acknowledgements

This thesis is dedicated to my parents.
Thank you Mom and Dad.

Table of Contents

List of Tables

List of Figures

xi

Chapter 1

Introduction

Fiber Bragg Grating (FBG) sensors are an attractive technology for measuring strain and temperature. FBG sensors are especially resilient in hazardous environments where traditional electronic sensors would not survive. These fiber optic sensors are resistant to electromagnetic interference, corrosive environments and fatigue [1]. Additionally certain fiber sensors can operate at temperatures exceeding 1745°C and can sustain strains of over 10% [2] [3].

The main focus of this thesis was to develop a method to embed FBG sensors into metallic structures for high temperature applications.

1.1   Motivation

FBG sensors can be externally fixed to structures to measure strain and temperature. External FBG sensors are readily available and can be used similarly to a resistive strain gages. Although measuring strain and temperature on the surface of a component is useful,

knowledge of the strain-temperature state of a component at arbitrary points inside the material is extremely valuable. Due to the geometry and toughness of FBGs, they are easier to embed than traditional resistive strain gages.

Embedding fiber optic sensors in concrete for structural health monitoring has been an active research area for several decades [4] [5] [1]. FBGs are attractive for civil engineering applications due to their ability to carry signals for long distances with minimal signal loss and their resistance to harsh corrosive environments.

More recently, researchers have examined the possibility of embedding FBG sensors in fiber composite parts[6] [7] [8]. Knowledge of the temperature-strain state of a critical fiber composite part is becoming increasingly valuable as the aerospace industry and the high performance automotive industry are adopting carbon fiber composite technology.

The main focus of this thesis, however, is to examine an effective procedure to embed FBG sensor in metallic components. Several different embedding techniques including ultrasonic consolidation and laser-based additive manufacturing have been used to embed FBGs into metallic structures [9]. Techniques for embedding FBGs in metals, however, are less mature than the techniques used to embed FBGs in concrete and in fiber composites.

The usefulness of FBGs to produce so called "smart" structures is especially clear in the aerospace industry [10]. Aerospace components such as turbine and compressor blades in turbine engines, landing gear forgings, pressurized fuselage panels, and hydraulic components are critical components subject to varying strain and temperature. The resistance to electromagnetic interference of FBGs is also becoming increasing valuable as many aircrafts are becoming more relient on electrically driven actuators throughout the airframe.

Embedded FBG sensors also has possible applications in the automotive industry. Recent legislation requires automotive companies to limit emissions by reducing weight [11].

This move towards lighter vehicles requires auto manufacturers to consider lighter structural materials such as aluminum and magnesium alloys. The use of embedded FBG sensors in the development and testing of components made from experimental alloys can provide internal stress, strain, and temperature data that was previously unattainable.

1.2 Challenges

The optical sensors discussed in this paper are based on Fiber Bragg Grating (FBG) sensor technology. FBGs are made by periodically modifying the refractive index at the core of optical fibers. Conventional FBGs are inscribed using UV laser irradiation, however, recently, femtosecond laser have been used to inscribe the grating for high temperature applications[2]. A diagram of an FBG is shown in Figure 1.1a.
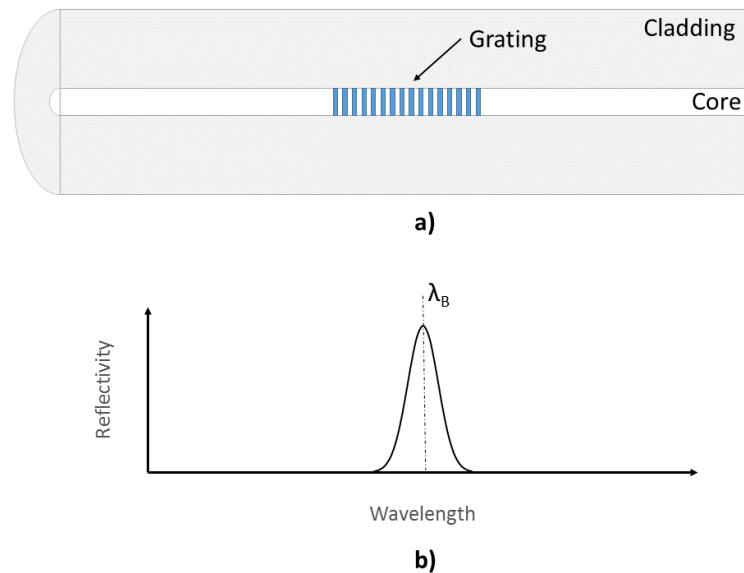
Figure 1.1: a) FBG diagram b) FBG reflectivity.

The grating inscribed in the fiber causes a specific wavelength of light to be reflected

3

back to the source [12]. This reflected wavelength is called the Bragg Wavelength (λ_B). The Bragg wavelength of a fiber can shift to a higher or lower wavelength depending on both the strain and temperature state of the fiber. The sensitivity of the Bragg wavelength to strain and temperature allows an FBG to be used as either a strain, a temperature sensor, or both.

One of the major challenges in using FBGs as sensors arises from the fact that the Bragg wavelength is sensitive to both strain and temperature. It is therefore difficult to differentiate if a shift in the Bragg wavelength is caused by a temperature change or an induced strain. The uncertainty related to this dual sensitivity must be mitigated if FBGs are to be used for practical applications.

For clarity, when an FBG sensor package design is only able to measure a single extrinsic property of a system (temperature OR strain) it will be called a "single-parameter" sensor. Single parameter sensors cannot determine the full temperature-strain state without external information. Usually single-parameters sensors are used to determine a single unknown parameter when others are known (i.e. measuring temperature under zero strain).

When an FBG sensor package design can measure two extrinsic properties of a system (temperature AND strain) it will be called a "dual-parameter" sensor. Design of dual-parameter FBG sensors requires careful consideration of many different areas of engineering. Modeling of optical, thermal, and mechanical effects must be done along with careful consideration of material properties to effectively produce a dual parameter sensor design. The additional requirement of embeddability further complicates the design of the dual-parameter sensor.

Another major challenge associated with embedding FBG sensors in metallic structures is the development of a feasible embedding process. Existing FBG metallic embed-

4

ding processes have significant restriction which limit their viability for use in real world applications. Several processes such as ultrasonic consolidation and laser based additive manufacturing require expensive specialized equipment and have limitations related to host part design [13] [14]. Embedding processes based on electrochemical deposition are slow and cannot be easily used to embed sensors within large structures [15]. Significant improvements on embedding techniques are needed before embedded FBG sensors can gain widespread use.

1.3   Objective

The main objectives of this thesis are as follows:

1. Develop an embedding procedure that can be used to embed FBGs into metallic structures.

2. Design a dual-parameter FBG sensor that can be embedded using the developed embedding procedure.

The objectives are supplemented by general desirable characteristics of the embedding procedure and the associated sensors:

- Existing components should be able to be retrofitted with these sensors. The embedding of the sensors should therefore be done after the manufacturing of host part rather than during the manufacturing of the host part,

- The practicality of the embedding procedure should be considered; expensive specialized equipment should be avoided and the embedding process should not be complex, time consuming, or expensive.

- The temperature of the embedding process should be low enough to try and avoid microstructural changes in the host material.

- The maximum operating temperature and strain of the sensors should be as high as possible to allow for broad applications.

- All FBGs and materials should be readily available and as few custom or exotic components should be used.

With these two main objectives and these general desired characteristics, an embedding process and the design of a dual-parameter sensor were developed

1.4   Contributions and Thesis Layout.

This thesis explores an alternative technique for embedding optical fiber sensors in metallic structures using drilling and low-temperature sintered silver nanoparticles an adhesive. Silver nanoparticle embedding has several advantages over previously attempted embedding techniques. Silver nanoparticle embedding requires no specialized equipment other than a temperature controlled sintering oven and standard machining equipment. It does not require the host part to be manufactured using any specific process. This embedding procedure does not use polymer adhesives which are prone to degradation at high temperatures. Moreover, this embedding procedure can be used to embed sensors at an arbitrary depth from the surface of the component.

Single parameter FBG sensors were embedded into metallic structures using the developed silver nanoparticle embedding procedure. The performance of the single parameter

sensors were characterized at various strains and temperatures. Additionally, a dual parameter sensor package using FBGs was designed and successfully embedded into a metallic structure. Preliminary characterization of the dual-parameter sensor design was carried out.

The thesis is separated into 5 chapters. This chapter introduced the motivation, challenges, objectives and the contributions of this thesis. Chapter 2 gives background information on optical fibers, FBGs, and existing embedding technologies. Chapter 3 describes the models used for the design of the embedding procedure for single and dual-parameter FBG sensors. Several design iterations for dual-parameter sensors are also described in Chapter 3. Chapter 4 contains the results of all characterization tests done on both single-parameter and dual-parameter embedded FBG sensors. Chapter 5 presents some discussion and conclusions about the performance of the embedded FBG sensors along with future work that can be done to improve the performance of embedded FBG sensors.

Chapter 2

Background Information

2.1   Optical Fibers and Fiber Bragg Gratings

Optical fibers are one of the most influential inventions of the 20th century. The advent of cheap and effective optical fibers in the 1980s revolutionized the telecommunications industry. The high bandwidth, low signal loss, and low cost of optical fibers as compared to copper wire brought forward the information age and made entirely new industries possible.

Although optical fibers are mainly used for data transmission, they can also be used as sensors. Due to the interesting properties of optical fiber sensors, their use in medicine and civil engineering is becoming more common [5][16][17].

This section will give an overview of optical fibers and how they can be used as sensors.

2.1.1 Optical Fibers

Snell's law describes how the interface of two materials with different refractive indices can redirect an incident light ray. Equation 2.1 describes the relationship between the refractive index of two materials (n_1, n_2), their angles of incidence (θ_1), and the angle of refraction (θ_2). Figure 2.1 shows a diagram of refraction and total internal reflection due to Snell's Law. Note that for Figure 2.1, the diagram assumes that $n_1 > n_2$.

$$\frac{sin(\theta_1)}{sin(\theta_2)} = \frac{n_2}{n_1} \tag{2.1}$$
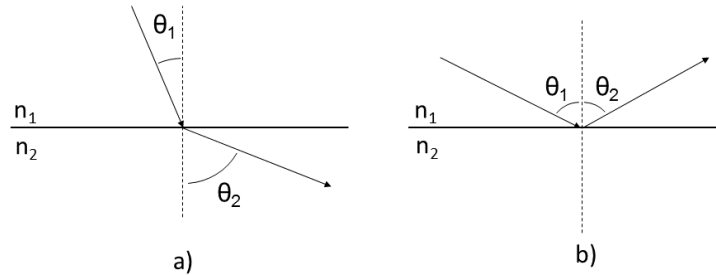
Figure 2.1: a) Refraction and b) total internal reflection described by Snell's law

Total internal reflection of a light ray in a material occurs when the incident angle exceed a critical angle ($\theta_1 > \theta_c$). This critical angle is described in Equation 2.2 [12].

$$\theta_c = arcsin(n_2/n_1) \tag{2.2}$$

Optical fibers are thin threads of optically clear material that exploit the effect of total internal reflection to transmit light with very low signal loss. Optical fibers are generally composed with a core and a cladding. The core has a higher index of refraction than the cladding to allow the total internal reflection of light.
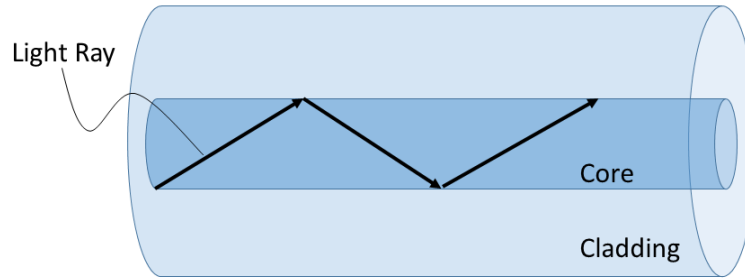
Figure 2.2: Total internal reflection of a light ray in an optical fiber.

Telecommunications optical fibers are commonly produced using silica glass. To produce the difference in the refractive index between the core and the cladding, dopants such as GeO_2 and P_2O_5 are often introduced in the glass during manufacturing [12].

2.1.2 Fibre Bragg Gratings

Fiber Bragg Gratings (FBGs) are optical fibers that have a grating inscribed in their core. Figure 2.3 shows a diagram of an FBG along with the refractive index of the core and the spectral response. In Figure 2.3, Λ is the grating pitch, n is the refractive index, P is power, and λ is the wavelength of light.

The grating in an FBG is simply a modulation of the refractive index (n) in the core of the fiber. Unmodified optical fibers transmit the majority of the light in the visible and near visible spectrum. By adding this grating, the transmission properties of the fiber are modified. A simple uniform FBG transmits most of the input light from a broad spectrum light source, however, a very specific wavelength of light will be reflected back to the source. The wavelength of the reflected light of an FBG is called the Bragg wavelength (λ_B).

FBGs produce this wavelength selective reflection by creating a Bragg condition at the grating. Each individual segment of the grating weakly reflects a small fraction of the

10
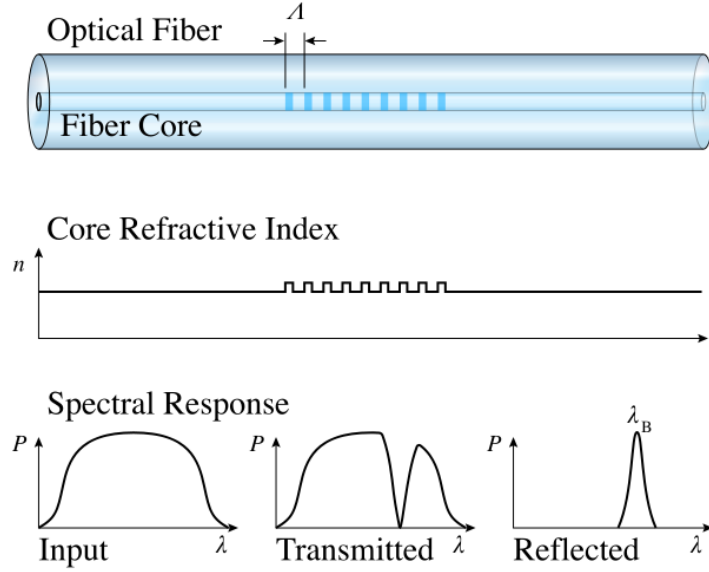
Figure 2.3: FBG with core refractive index and spectral response [18].

entire input spectrum. The grating causes a single wavelength to constructively interfere based on the pitch of the grating and the effective refractive index of the core. Equation 2.3 describes the relationship between the Bragg wavelegth, the grating pitch and the effective index of refraction of the grating (n_{eff}) [12].

$$\lambda_B = 2n_{eff}\Lambda \qquad (2.3)$$

2.1.3 FBGs as Sensors

The refractive index and the pitch of the grating can change by exposing the fiber to different temperatures and strains. As temperature increases, the optical properties of the core change and the grating pitch is widened due to thermal expansion. Similarly, as strain on the fiber increases both the refractive index of the core and the pitch of the grating will

11

change. More detailed models for determining the Bragg wavelength and the reflectivity spectrum of an FBG are described in Section 3.1.

When an FBG sensor package design is only able to measure a single extrinsic property of a system (temperature OR strain) it will be called a "single-parameter" sensor. Single parameter sensors cannot determine the full temperature-strain state without external information. Usually single-parameters sensors are used to determine a single unknown parameter when others are known (i.e. measuring temperature under zero strain).

A plain FBG as shown in Figure 2.3 is an example of a single-parameter sensor. The Bragg wavelength shift from the FBG in Figure 2.3 can be caused by either a temperature change or strain.

The development of dual-parameter FBG sensors is an active area of research. Several approaches in producing a dual parameter sensor from FBGs have been attempted. Xie et al. [19] used cantilevered steel plates and epoxy to produce dual parameter effects with uniform FBGs. Liu et al. [20] used tapered FBGs along with microfiber cavities to produce dual-parameter sensors. Alemohammad et al. [21] used a silver thin film superstructure on a uniform FBG to create a dual-parameter sensor. Liang [22] used epoxy, hypodermic needle sheaths, and uniform FBGs to produce a dual parameter sensor. The design of dual-parameter sensors in this thesis were based on the work in [22]. More detailed descriptions of existing dual-parameter sensors and the the design process of the dual-parameter sensors developed in this thesis can be found in Section 3.3.3.

2.2 Embedding Technologies

One of the main objective of this thesis was to embed FBG sensors into metallic structures. Many different embedding techniques have been attempted by researchers with varying degrees of success and practicality. This section will explore a selection of embedding techniques that were considered.

2.2.1 Ultrasonic Additive Manufacturing

Ultrasonic welding (USW) is a solid state welding method similar to friction welding or explosion welding. Ultrasonic welding uses ultrasonic vibration to bond two pieces of material together. Generally, ultrasonic welding is used to bond relatively thin sheets of plastics or metals [23]. Figure 2.4 shows a diagram of an ultrasonic welding setup.
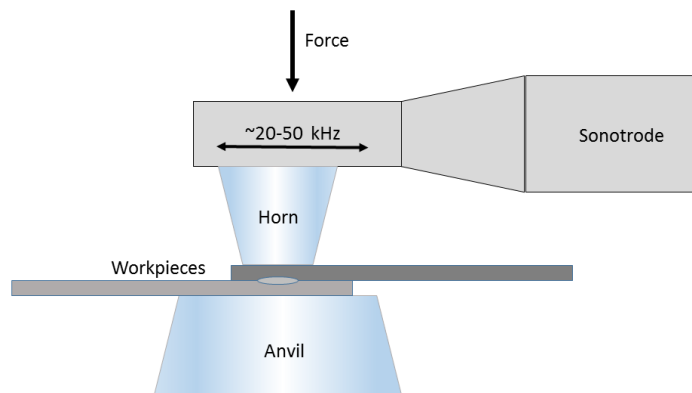
Figure 2.4: Ultrasonic Welding Diagram.

The sonotrode is the source of the ultrasonic energy. Sonotrodes commonly use piezoelectric elements or pneumatic elements to produce the ultrasonic waves. The waves are then then passed through boosters to modify the amplitude of the vibration. Once the

vibrations reach the horn, they usually have an amplitude of 15-60 μm at a frequency between 20-50 kHz [24].

Force is applied on the horn perpendicular to the amplitude of vibration. The combination of pressure and vibration energy welds the two workpieces together. The exact bonding mechanism that produces the weld is still under debate; interdiffusion, recrystallization, plastic deformation, work hardening, breaking of contaminants, friction heat generation, and melting have been proposed as possible mechanisms [24].

A combination of ultrasonic seam welding and computer numerically controlled machining has been used to produce three dimensional objects, this process has been called Ultrasonic Additive Manufacturing (UAM) or ultrasonic consolidation [24]. Fabrisonic LLC (Columbus, Ohio) is currently one of the few companies offering UAM machines commercially [25].

UAM has been used by several researchers to embed optical fibers and FBGs into metallic substrates. Li et al. [26] [27] used UAM to embed SiC fiber in a Al 6061 and Al3003 matrices. Zhu et al. [13] used a combination of electroless plating and UAM to embed FBGs into an Al 6061 matrix. Li et al [28] used a similar technique of electroplating and ultrasonic spot welding to embed FBGs in copper and aluminum matrices.

USW is an attractive method of embedding FBGs for a few important reasons. First, embedding of FBGs using USW and UAM has been successfully demonstrated. USW is a fast process, a single ultrasonic weld can be completed on the order of seconds. USW is a low temperature process. The heat affected zone of a USW in AA6111-T4 has been shown to have a maximum temperature of around 500 °C with a temperature below 200°C after 1 second of welding [29].

Although USW and UAM are attractive methods for embedding FBGs into metallic

14

structures, there are some drawbacks to this embedding method. USW and especially UAM machines are expensive and specialized equipment. Additionally, UAM cannot be used to retrofit an existing component with an embedded FBG. Using UAM, the FBG must either be embedded at the surface of the existing component or the component must be built around the FBG.

2.2.2   Cold Spray Embedding

Cold spray was briefly considered as a technique for embedding FBGs. Cold spray, also known as "kinetic spraying" or "high-velocity powder deposition", is a material deposition process that uses particles accelerated to a high velocity to produce a coating on a substrate. The particles range from 1-50 μm in diameter and are accelerated up to 1200 m/s before impacting the substrate. The high velocities are usually achieved by using a high velocity inert carrier gas stream. The process is called cold spray because the gas temperatures usually range from 0 to 700°C. This temperature is usually below the melting point of the coating material. The high velocity particles impinge the surface of the substrate and bond to the substrate due to severe plastic deformation[30].

Cold spray has a few properties that make it an attractive process for embedding FBGs. First, cold spray is a solid state process with relatively low temperatures. Cold spray is also a high speed deposition process that can produce arbitrarily thick coating layers.

The most obvious disadvantage of using cold spray as an embedding method is the aggressive nature of the process. Due to the high velocity of the carrier gas and the plastic deformation of the impinging particles, an exposed FBG would likely be destroyed instantly.

2.2.3 Laser Based Additive Manufacturing

Laser based metal additive manufacturing is a manufacturing process that can produce three dimensional components in a layer-by-layer fashion. Two categories of additive manufacturing(AM) that are of interest for embedding FBG sensors are Laser Engineered Net Shaping (LENS) and Selective Laser Melting (SLM). Figure 2.5 shows a simplified representation of both LENS and SLM.
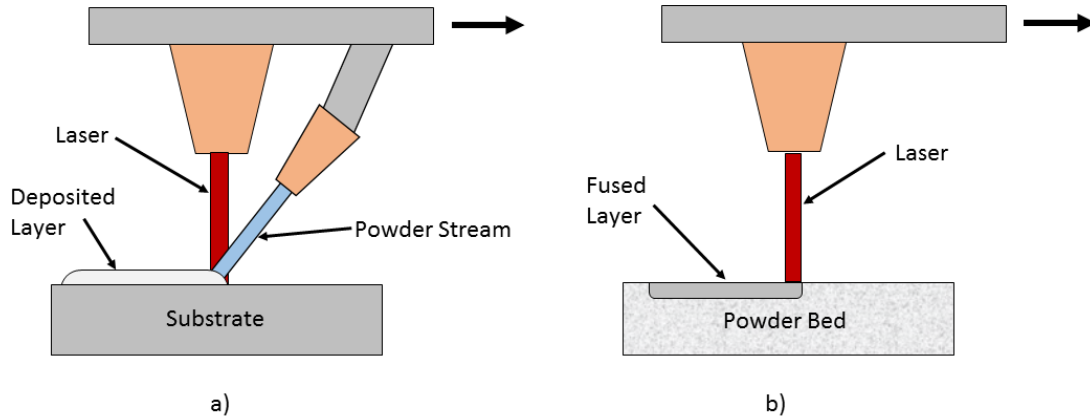
Figure 2.5: a)LENS with lateral nozzle. b)SLM

Both LENS and SLM processes use a laser as an energy source and primarily use metallic powders as a feedstock material. Both processes also use a Computer Numerically Controlled (CNC) stage to direct the laser energy to build a single layer of a component. LENS uses an inert carrier gas to spray the metallic powder into the melt pool while SLM selectively melts portions of a powder bed to produce a layer. Once a single layer has been produced, a subsequent layer is deposited/fused above the previous one. Note that SLM requires an additional layer of powder to be deposited before the next layer can be fused. The layer deposition process is repeated until the desired three dimensional component is completed.

16

LENS and SLM along with various other laser based AM processes have been used to produce components with embedded FBGs. The general approach to embed an FBG with these laser AM methods is to build the metallic component around the FBG. Havermann et al. [31] and Maier et al. [14] used SLM to embed FBGs into SS 316. Li et al. used LENS to embed nickel electroplated FBGs int SS 316. Alemmohamad et al. [15] used a combination of electroplating, laser assisted maskless microdeposition and LENS to produce a tungsten carbide-cobalt machine tool with and embedded FBG.

Laser AM has been shown as an effective method for embedding fibers, however, there are a few disadvantages. Laser AM machines are expensive and specialized pieces of equipment. Similarly to ultrasonic embedding, fibers can only be embedded at the surface of existing components unless the entire component is "built" around the sensor using laser AM.

2.2.4 Epoxy Embedding

Epoxy embedding is a method of embedding FBG sensors using epoxy resins. Epoxies are frequently used as a in fiber composite materials. The embedding of FBG sensors in epoxy has been shown as an effective method for measuring strain development during the curing of epoxy [6] [32] [33] [34]. Epoxy is also used to adhere FBGs to metallic encapsulations in strain and temperature sensors for structural health monitoring in civil engineering [35] [4]. Epoxy embedding, however, has rarely been used to embed FBG sensors for strain and temperature monitoring in metallic components.

Figure 2.6 shows a cross-section of an FBG embedded into a metallic host part with epoxy as the adhesive.

The embedding procedure for embedding an FBG into a metallic component using

17
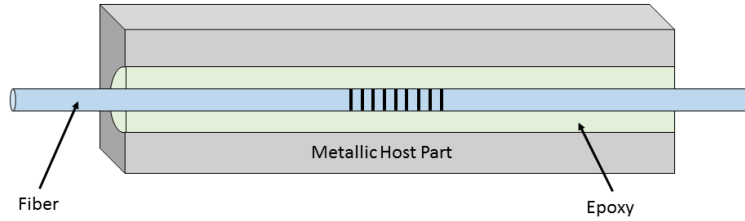
Figure 2.6: Cross-section of FBG Embedded in Metallic Host Part with Epoxy

epoxy is simple. First, the host part must be manufactured with a channel to accept the fiber or the channel must be machined into the part post-manufacturing. The fiber is then inserted into the channel along with epoxy resin. The epoxy is then thermally cured.

This embedding method requires no specialized equipment other than standard machine tools and a temperature controlled heat source. Epoxy embedding can also be used to retrofit parts that have not specifically been designed to accept embedded FBG sensors regardless of the manufacturing procedure used to produce the host part.

The main disadvantage of epoxy embedding is the performance of the epoxy resin at higher temperature. Epoxy resins are susceptible to oxidation at higher temperatures and important mechanical properties such as tensile strength may begin to degrade[36]. For example, Aremco 805 ultra high temperature epoxy has a rated temperature resistance of 300°C [37]. This temperature performance may not be acceptable for certain high temperature applications.

2.2.5 Summary

The two main objectives proposed in this thesis are as follows:

1. Develop an embedding procedure that can be used to embed FBGs into metallic structures.

18

2. Design a dual-parameter FBG sensor that can be embedded using the developed embedding procedure.

Although FBG embedding procedures and dual-parameter sensors have been studied, there is no existing literature proposing the use of silver nanoparticle paste as the main adhesive for FBG embedding. All existing procedures either require specialized, expensive equipment or have poor performance at higher temperature.

This novel embedding procedure requires no specialized equipment and allows any metallic part to be retrofitted with embedded sensors. FBGs embedded using silver nanoparticle paste also has the potential to perform better at higher temperatures than FBGs embedded using polymeric adhesives.

In this thesis, an embedding procedure using silver nanoparticles is developed. A new design for dual parameter sensors was also developed in conjunction with the silver nanoparticle embedding procedure. The novel embedding procedure and the associated dual-parameter sensor design are the main contributions of this thesis.

Chapter 3

Modelling and Design

3.1 Modeling

There are three analytical models used in this paper to predict the behaviour of embedded FBGs. The first model was used to predict how the strain in the host material is transfered to a fiber. The second model was used to correlate the temperature and strain sensitivity of the embedded FBG to the recorded Bragg Wavelength. The third model is used to predict the reflectivity spectrum of an FBG which may be under non-uniform strain distribution.

3.1.1 Strain transfer analysis of embedded fibers

The analytical model used to predict the strain distribution along an embedded fiber was based on the work by F. Ansari et al.[38] [39].

Figure 3.1 shows the graphical representation of the model. Note that Figure 3.1 is a cross section that must be revolved and mirrored to describe the whole system. The

bonded length of fiber is $2L$, r represents radial dimensions, σ represents linear stress, τ represents shear stress, and ϵ represents linear strain along the x axis.
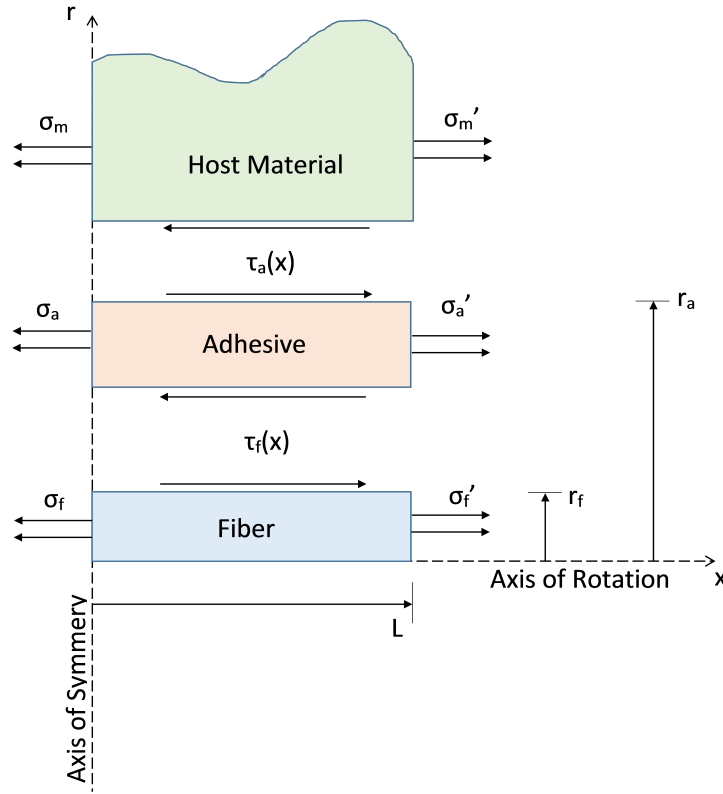
Figure 3.1: Strain transfer model for embedded fibers.

The material properties used in this analysis are the elastic modulus E and the shear modulus G.

Subscripts on any variable in the paper are used to specify the material in question. The subscript f is for the fiber, a is for the adhesive, and m is for the host material.

The analysis is based on strain transfer theory. The assumptions and boundary conditions for this model will be outlined.

Assumptions:

1. All material behaves in a linear elastic manner.

2. There is a perfect bonding between each material layer. $\epsilon_f(r_f) = \epsilon_a(r_f)$, $\epsilon_a(r_a) = \epsilon_m(r_a)$

3. The mechanical properties of the fiber core and cladding are the same.

4. The bonded length L is significantly longer than the radius of the fiber. $(r^2 - r_f^2)/L \approx 0$

Boundary conditions:

1. There is no stress at the end of the fiber or the adhesive. $\sigma'_f = 0$, $\sigma'_a = 0$

2. The shear stress should be zero at axes of symmetry.

3. The strain in the fiber and the strain in the host material are equivalent at the axis of symmetry. $\epsilon_f(0) = \epsilon_m(0)$

By using force equilibria and Hooke's law, the following relationship between the strain in the host material and strain in the fiber can be derived. This derivation is shown in detail in [38].

$$k^2 = \frac{2G_a}{r_f^2 E_f ln(r_a/r_f)} \tag{3.1}$$

$$\frac{\epsilon_f(x)}{\epsilon_m} = 1 - \frac{sinh(kx)}{sinh(kL)} \tag{3.2}$$

22

Equation [3.2](#) describes an important property in designing embedded FBG sensors. $\frac{\epsilon_f(x)}{\epsilon_m}$ is called the strain transfer ratio. It is the ratio between the strain on the fiber relative to the strain of the host material. If the goal of the embedded FBG is to measure the strain in the host material, a strain transfer ratio of 1 would be ideal. However, if the goal of an embedded FBG is to solely measure temperature, a strain transfer ratio of 0 would be better.

3.1.2 Simplified Optomechanical Model of FBG

The purpose of the optomechanical model is to correlate the temperature and strain sensitivity of the fiber to the Bragg wavelength shift of the FBG. This relationship is described in Equation [3.3](#) where λ_0 is center Bragg wavelength, $\Delta\lambda_B$ is the shift in Bragg Wavelength, ϵ is the strain on the fiber and Δ_T is the change in temperature.

The shift in Bragg wavelength ($\Delta\lambda_B$) is a linear combination of strain on the fiber (ϵ) and temperature change (ΔT). The scalars of this linear combination are the wavelength-strain coefficient γ, the wavelength temperature coefficient ϕ.

$$\Delta\lambda_B = \gamma\Delta\epsilon + \phi\Delta T \tag{3.3}$$

The γ coefficient relates the effect of axial strain on the fiber to the corresponding shift in Bragg wavelength. In Equation [3.3](#), ϵ only refers to the mechanically induced strain. For this model, the wavelength-strain coefficient will be described for simple uniaxial strain using Equation [3.4](#) where p_e is the photo elastic constant along the length of the fiber.

$$\gamma = \lambda_0(1 - p_e) \tag{3.4}$$

Equation 3.5 describes the wavelength-temperature coefficient ϕ. Temperature has two main effects on the Bragg wavelength shift. The fiber's refractive index change caused by temperature changes is described by the thermo-optic coefficient β_Λ. The effect of thermal expansion is described by the coefficient of thermal expansion of the host material α_h and the wavelength-strain coefficient γ. Equation 3.5 assumes that there is perfect strain matching between the host material and the fiber.

$$\phi = \lambda_0 \beta_\Lambda + \alpha_h \gamma \tag{3.5}$$

The thermo-optic coefficient can be determined from the effective refractive index of the fiber (n_{eff}) and the fiber's thermal coefficient of index of refraction (dn/dt). Equation 3.6 shows this relation.

$$\beta_\Lambda = \frac{1}{n_{eff}} \left(\frac{dn}{dt} \right) \tag{3.6}$$

To obtain a complete model of the FBG from material properties, Equations 3,4,and 5 can be combined

$$\Delta \lambda_B = \lambda_0 (1 - p_e) \Delta \epsilon + \lambda_0 \left(\frac{1}{n_{eff}} \left(\frac{dn}{dt} \right) + \alpha_h (1 - p_e) \right) \Delta T \tag{3.7}$$

The scalar values γ and ϕ can be determined analytically from known optical and materials properties, they can also be determined through sensor calibration.

3.1.3 Optomechanical Model of FBG with Non-Uniform Strain Distribution

The model in Section 3.1.2 is only valid for uniform gratings with a uniform strain distribution along the fiber axis. In this thesis, FBGs will be exhibited to non-uniform strain distributions. It is therefore necessary to be able to predict the reflected spectrum from a uniform FBG which is under non-uniform strain along the length of the grating. We will, however, assume that all gratings have a uniform temperature distribution.

Coupled mode theory will be used to produce an optical spectrum for FBGs under non-uniform strain distributions. The derivation of the optomechanical model is based on the work of Ling et al. [40].

The following three parameters of the FBG must be known. The first parameter is the strain free wavelength λ_0. This λ_0 parameter is the Bragg wavelength of the fiber at room temperature and under no strain. The second parameter is the effective index of refraction of the fiber core n_{eff}. The third parameter is the pitch of the grating at room temperature under no strain Λ_0. If two of these parameters are known, the third can be found using Equation 2.3.

The DC index change spacially averaged over the entire grating $(\overline{\delta n_{eff}})$ and the fringe visiblity (ν) of the the grating must be known.

Using the known fiber properties, the DC coupling coefficient $(\hat{\sigma})$ and the AC coupling coefficient (κ) can be found using Equations 3.8 and 3.9. For the following Equations, λ is the wavelength variable and z is the variable representing the position along the length of the grating. The total length of the grating is L where $-L/2 \leq z \leq L/2$.

$$\hat{\sigma}(z) = 2\pi n_{eff} \left(\frac{1}{\lambda} - \frac{1}{\lambda_B(z)} \right) + \frac{2\pi}{\lambda} \overline{\delta n_{eff}} \tag{3.8}$$

$$\kappa(\lambda) = \frac{\pi}{\lambda} \nu \overline{\delta n_{eff}} \tag{3.9}$$

$\lambda_B(z)$ is the strain-modified Bragg wavelength which is described in Equation 3.10 where $\epsilon(z)$ is the strain along the length of the FBG.

$$\lambda_B(z) = \lambda_0(1 + (1 - p_e)\epsilon(z)) \tag{3.10}$$

The amplitude of the forward and backward propagating modes are $R(z)$ and $S(z)$ respectively.

$$\frac{dR(z)}{dz} = i\hat{\sigma}R(z) + i\kappa S(z) \tag{3.11}$$

$$\frac{dS(z)}{dz} = -i\hat{\sigma}S(z) - i\kappa R(z) \tag{3.12}$$

The reflectivity of the FBG with respect to the wavelength ($f(\lambda)$) can be determined.

$$f(\lambda) = \left| \frac{S(-L/2)}{R(-L/2)} \right|^2 \tag{3.13}$$

The main challenge when trying to find the reflectivity spectrum of the FBG is solving the first-order differential equations for the forward and back propagating modes. Numerical solutions can be found using the Runge-Kutta method, however a piecewise-uniform approach is generally faster to compute and easier to implement [41].

In the piecewise-uniform approach, the grating is divided lengthwise into M sections with length of Δz which are each subject to uniform strain. To allow for proper coupling, the number of sections must be constrained as follows.

$$M << \frac{2n_{eff}L}{\lambda_0} \tag{3.14}$$

A T-matrix formulation is then used to find the propagation modes at one end of the grating.

$$\begin{bmatrix} R(-L/2) \\ S(-L/2) \end{bmatrix} = F \begin{bmatrix} R(L/2) \\ S(L/2) \end{bmatrix} \tag{3.15}$$

Where F is defined as

$$F = F_M \cdot F_{M-1} \cdot F_{M-2} \cdots F_1 \tag{3.16}$$

$$F_i = \begin{bmatrix} cosh(\gamma_B \Delta z) - i\frac{\hat{\sigma}}{\gamma_B}sinh(\gamma_B \Delta z) & -i\frac{\kappa}{\gamma_B}sinh(\gamma_B \Delta z) \\ i\frac{\kappa}{\gamma_B}sinh(\gamma_B \Delta z) & cosh(\gamma_B \Delta z) + i\frac{\hat{\sigma}}{\gamma_B}sinh(\gamma_B \Delta z) \end{bmatrix} \tag{3.17}$$

$$\gamma_B = \sqrt{\kappa^2 - \hat{\sigma}^2} \tag{3.18}$$

Appendix A shows an implementation of this optomechanical model in Matlab.

3.2   Materials and Bonding

The embedded FBG sensor system consists of three main components: the fiber, the adhesive, and the host material. If these sensors are to be embedded into a variety of materials, the properties of the host material should not be modifiable. Similarly, if standard optical fibers are being used, their properties cannot be modified. It is therefore critical to carefully select the intermediate adhesive and to design an effective embedding procedure that can be applied as a general solution for embedded sensors in metallic components.

Epoxy is traditionally used as an adhesive for optical fibers in various sensor packages and in the telecommunications industry. Epoxy has also been used for embedding FBGs in fiber composite materials [42]. Although epoxy can be an effective adhesive for low temperature applications, epoxies produce unwanted sensor drift and debonding at higher temperature [22]. Furthermore, polymer based epoxies rarely have the desired combination of physical and mechanical properties required for embedded sensor applications. A successful adhesive must have the following general characteristics:

1. Good bonding strength with both silica glass and metallic substrate.

2. Wide range of operating temperatures.

3. Modulus low enough to not bias the strain from the host material but high enough to effectively transfer the host material strain.

4. Able to sustain large strains.

To embed optical fibers, a metallic based adhesive was used instead of a polymer based adhesive. A combination of silver nanoparticle ink and paste was used in the embedding

procedure. This section will focus on the properties of the fiber, the adhesive, and the host material. Interaction of the silver based adhesive with the host material and the optical fiber will be examined. This section will also describe the sintering schedule for silver nanoparticle paste.

3.2.1 Fibers

Two different types of FBGs were used in this paper. For all tensile tests below $300°C$, Corning SMF-28 Germanium doped single mode fibers were used. The gratings were inscribed into these fibers using a UV laser. These low temperature fibers had a maximum operating temperature of $300°C$.

For the tensile tests above $300°C$ and all repeatability tests, FiberCore SM1250SC(10/125)P pure silica fibers were used. The gratings for the high temperature FBGs were inscribed using a femtosecond laser.

Although there are doping elements in the glass fibers, the mechanical properties of the fibers was assumed to be the same as pure fused silica. Table 3.1 shows the important properties of the FBGs used in the paper.

3.2.2 Host Material

For all tests conducted, the host material used was 4mm thick AZ31B-H24 sheet. All samples were cut along the rolling direction and followed the ASTM E8 standard for sample geometry. To accommodate the fibers, a square channel was machined at the surface of the sample. Engineering drawings for the samples can be found in Appendix B.

Table 3.1: Mechanical and optical properties of FBGs.

Property	Value	Unit
Radius(r_f)	62.5	μm
Grating Length(L_G)	5.0	mm
Elastic Modulus(E_f)	73.1	GPa
Center Wavelength (λ_0)	1530	nm
Thermal Coefficient of Index(dn/dt)[43]	11×10^{-6}	$^{\circ}C^{-1}$
Strain-Optic Coefficient(p_e)	0.22	
Effective index of Refraction(n_{eff})	1.444	

Although the composition of host material affects the bonding strength of the adhesive, the only important physical property of the host material to model the behaviour of an embedded FBG sensor is the coefficient of thermal expansion. For this paper, a constant value of 26 μm/m$^{\circ}$C will be used as the coefficient of thermal expansion of the host material.

3.2.3 Silver Adhesive

Two silver adhesives were used in the embedding process, Novacetrix JS-B40G high viscosity silver nanoparticle ink and NBE Tech silver nanoparticle paste.

Silver nanoparticle inks and pastes used in this study have silver nanoparticles in the 30-80 μm range [44][45]. These nanoparticle pastes also contain dispersants, solvents, and binders to help prevent particle clumping and premature sintering[46]. All additives in the paste are vaporized during the sintering process and only silver remains in the adhesive layer. The main advantage of using silver nanoparticles as an adhesive is the low sintering temperatures of the paste and the high temperature performance of the sintered silver. The properties of the silver paste are outlined in Table 3.2.

The shear modulus of the silver paste was not defined in the manufacturer specifications.

Table 3.2: Properties of silver nanoparticle paste[47].

Property Before Sintering	Value	Unit
Solid Loading	71-91	%
Sintering Temperature	>260	°C

Property After Sintering	Value	Unit
Porosity	<30	%
Melting Temperature	961	°C
Elastic Modulus	10-30	GPa

For modelling purposes, the Poisson's ratio of bulk silver (0.37) will be used. If an elastic modulus of 15 GPa is used, shear modulus can then be determined to be 5.5 GPa.

3.2.4   Sintering Schedule

The purpose of the sintering schedule is twofold. First, all solvents, binders, and dispersants must be evaporated. Second, the bare silver nanoparticles must then be sintered.

The manufacturer recommended sintering schedule involves a 5-7 °C/min ramp up to 260 °C and a 5-30 min soaking period [47]. The manufacturer recommended schedule produced significant cracking in the adhesive layer. To reduce cracking a modified sintering schedule based on the work of Wang et al. was used [45]. This schedule is shown in Figure 3.2.

The samples in this study had open 200-800 μm square channels filled with silver paste. For applications where larger volumes of silver paste are required, the soaking times at 50, 100, and 180 °C should be longer do allow all volatile additives to fully evaporate. Failure to evaporate all additives before increasing the temperature may result in paste boiling, significant porosity, and poor adhesive strength.
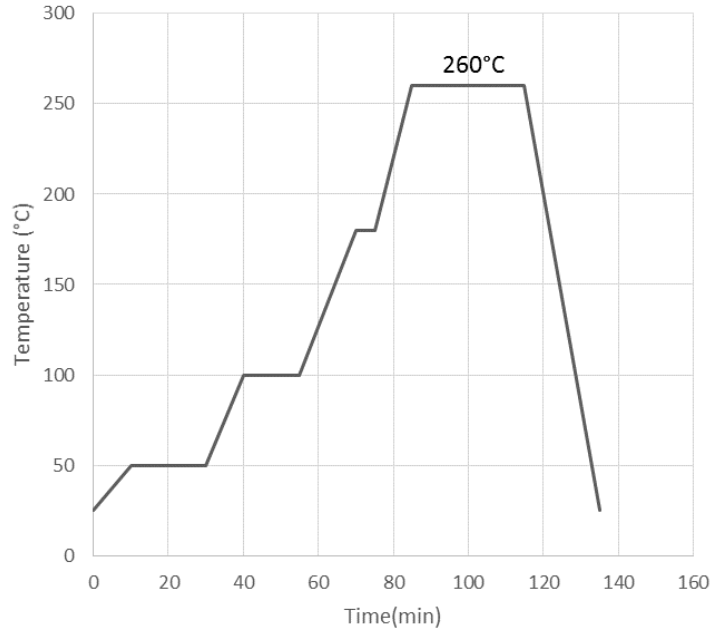
Figure 3.2: Sintering schedule.

3.2.5 Bond Performance

The bonding strength of the silver nanoparticles to the AZ31B sample and the glass fibers were not independently measured in this study. The performance of the embedded FBG sensor was instead characterized as a whole. In this section, the properties of the bonding interfaces will be briefly examined based on literature.

There are two important interfaces in the embedded sensor package. The bonding layer between the silver adhesive and the optical fiber and the bonding layer between the silver adhesive and the magnesium alloy. The performance of these bonding interfaces can be examined separately.

The silver-fiber bond is a glass-metal bond. To produce a good glass-metal bond, there are two critical criteria outlined by ASM [48]. First, atomic level contact is necessary

between the glass and the metal. Second, chemical bonding between the glass and the metal to form is necessary. An oxide layer forms between the glass and the metal through diffusion and stabilizes the bond. The bond between SiO_2 and Ag is formed when the Ag comes in contact with the SiO_2. Ag_2O is dissolved in the glass and a silver silicate interlayer is formed between the glass and the silver[49].

The bond between the silver and the AZ31B magnesium alloy is a simple metal-metal bond. No literature was found on the bond performance of silver to AZ31B, however, the Ag-Mg binary alloy system has been examined [50]. The solubility of Ag in Mg is limited, however, the solubility of Mg in Ag is extensive. Wang et al. have studied the performance of diffusion bonding between Mg-Ag-Al joints and have shown that ductile intermetallics form between the Ag and Mg[51]. They have also shown that the maximum temperature of the Ag-Mg interface is 470 °C and it has a minimum bonding shear strength of 11.8 MPa.

Shrinkage is problematic while using silver nanoparticles as an adhesive. Significant shrinkage occurs during the sintering process even with a high silver content paste. NBE nano-silver paste has been shown to shrink by 40% due to evaporation of binder and by 10% due to silver densification [45]. If excessive shrinkage occurs during the sintering process, delamination at the bond interface and cracking can occur and will produce poor bond performance. Figure 3.3 shows shrinkage cracking of silver nanoparticle paste in a square channel. Care should be taken during the design of embedded sensors to avoid cracking.
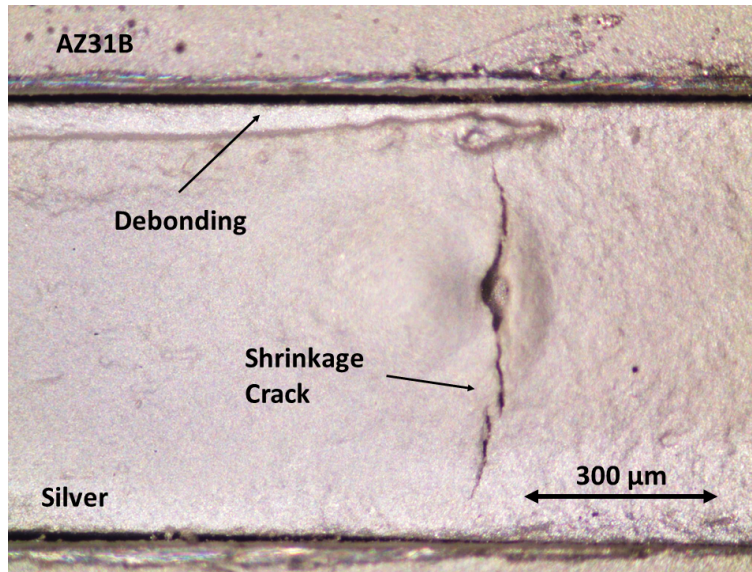
Figure 3.3: Silver nanoparticle paste debonding and cracking due to shrinkage.

3.3   Embedded Sensor Design

3.3.1   Embedded Single Parameter Sensor Design

The embedded single parameter sensor design in this thesis is nearly identical to an the epoxy embedded FBG described in section 2.2.4. Instead of using an epoxy as the adhesive, silver nanoparticle paste is used as an adhesive.

The length of the embedded section of fiber is critical to the performance of the embedded sensor as a whole. The geometry of the embedded sensor and the expected sensor performance will be determined from the models described in this study.

To have a successful embedded sensor design, the transfer of axial strain from the host material to the fiber must be exceptional. The strain transfer can be determined from Equations 3.1 and 3.2 along with Tables 3.1 and 3.2. Figure 3.4 shows the strain transfer ratio along the length of a 5mm long FBG. The total length of the embedded section is
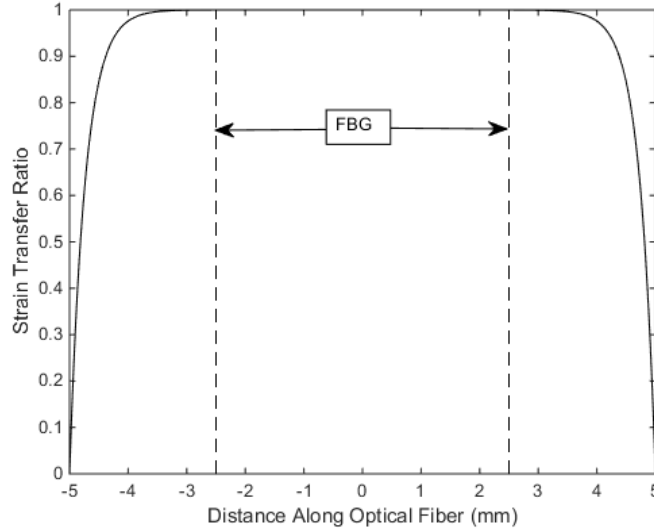
Figure 3.4: Strain transfer ratio along an embedded FBG.

10mm and the diameter of the hole is 200 μm.

Figure 3.4 shows that the strain transfer from the host material to the fiber is 100% as long as the FBG has at least 2.5 mm of embedded plain fiber at each end. It is important to note that the minimum length of the plain fiber ends is dependent on the mechanical properties and the geometry of the fiber and the adhesive. Although 2.5mm of embedded plain fiber should be sufficient, all test samples made had at least 10mm of embedded plain fiber at each end of the FBG to ensure 100% strain matching.

The sensitivity of the embedded FBGs can be calculated from Equations 3.4 and 3.5 along with Tables 3.1 and 3.2. The optical interrogator being used in this study is a Micron Optics sm125-200 with a wavelength accuracy of 10 pm and a repeatability of 1 pm [52]. The performance of the embedded FBG sensor is outlined in Table 3.3.

Table 3.3: Theoretical performance single parameter FBG sensor embedded in AZ31B.

	Sensitivity	Accuracy	Repeatability
Temperature(°C)	42.7 pm/°C	0.2 °C	0.02 °C
Strain ($\mu\epsilon$)	1.19 pm/$\mu\epsilon$	8 $\mu\epsilon$	0.8 $\mu\epsilon$

3.3.2 Embedding Procedure

The fiber embedding procedure can be broken down into three steps.

1. The first step involves cleaning the fibers and doing surface preparation on the host material.

2. The second step is the silver ink precoat.

3. The third step is the silver paste bonding.

These three steps will be explained in detail.

Surface Preparation

The surfaces of the host material and of the fiber must be cleaned and prepared to produce the best bond strength.

The optical fibers are often coated with a protective polymer layer. The purpose of this layer is to protect the fused silica fiber from damage during handling. The most common polymers used for fiber coating are polyacrylate or polyimide. If the fiber is being embedded using silver based adhesives, the polymer layer must be removed prior to any application of silver.

Mechanical stripping methods can be used to remove polyacrylate coatings but these methods usually damage the surface of the silica fiber and reduce the strength of the fiber. To avoid any weakening of the fiber, chemichal stripping was used instead of mechanical stripping.

Sulfuric acid with 96% concentration was used to remove the polyimide coatings of all FBGs. The sulfuric acid stripping method from M. Matthewson et al was used[53].

To remove FBGs with polyacrylate coating Recochem brand furniture stipper was used. The furniture stripper contained between 70-90% w/w methylene chloride, 5-10% w/w methanol, and 1-5% w/w toluene. The furniture stripper was applied to the surface of the fiber at room temperature and allowed to rest for 5 minutes. The softened polyacrylate was then removed with cotton swabs while avoiding touching the glass surface of the fiber. The fiber was then rinsed with isopropanol.

The test specimens were made from AZ31B-H24 sheet with a 200 μm square channel. Before embedding the FBGs in the channel, the surface of the specimen was roughed with a steel wire brush. The specimens were then ultrasonically cleaned in an acetone bath for 15 minutes to remove the remaining dirt and grease from the specimen.

Silver Pre-coat

When sintering silver nanoparticle paste, shrinkage cracking and delamination from the host material can be problematic while using the paste as a bulk adhesive. Figure 3.3 shows shrinkage cracks produced in a sample with a 700 μm square channel. The geometry of the channel causes the silver paste to delaminate from the surface as paste additives are evaporating.

To improve the bonding of the silver paste to the host material and the fiber, a thin

layer of silver nanoparticle ink is deposited and sintered on both the fiber and the in the channel of the specimen before the fiber is embedded in the sample. The silver ink is then sintered using the schedule described in Section 3.2.4.

The rational for using a silver pre-coat on the fiber and the host material is to separate the formation of the Ag-Mg bond and the Ag-Glass bond from the severe paste shrinkage during the formation of the bulk adhesive layer.

Silver Bonding

Once the silver pre-coat is applied, the fiber can now be embedded in the sample using silver nanoparticle paste. A 20 mm section of the channel of the sample is filled with silver paste. The FBG is then delicately placed at the center of the filled section of the channel. The entire sample is sintered using the schedule described in Section 3.2.4.

3.3.3 Embedded Dual Parameter Sensor Design

Several designs were considered during the development of a working embeddable dual parameter sensor. These designs used combinations of ultrasonic embedding, embedded reinforcements, different adhesive types, and multiple fiber arrangements. First, the design of an external dual parameter sensor will be examined. The three most viable dual parameter sensor designs will then be examined. The three embedded dual parameter designs are all based on the silver nanoparticle embedding method. For readability, 'embedded dual parameter sensor' will be shortened to EDPS.

Single Needle External Dual Parameter Sensor

The first design for an EDPS using silver nanoparticle adhesive was based on the work of T.Y.R. Liang [22]. In [22], a dual parameter FBG sensor was developed using epoxy and a hypodermic needle. This dual parameter sensor was not embedded, it was intended to be used externally. Figure 3.5 shows a cross section of the sensor developed in [22].
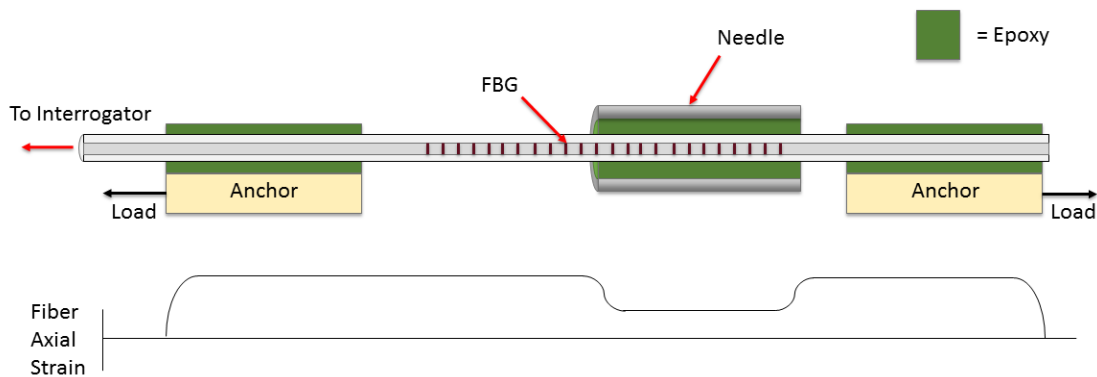
Figure 3.5: External dual parameter sensor developed by [22].

The idea behind the sensor in Figure 3.5 is to create two distinct regions on the FBG. Half of the FBG is encapsulated by a sheath made from a hypodermic needle. This needle is adhered to the fiber using epoxy as an adhesive. The two ends of the fiber are attached to anchors using epoxy. The anchors are used to load the fiber and to induce a strain on the fiber.

The two halves of the FBG react differently when a load is applied to the anchors. The FBG section with the needle is stiffer relative to the FBG section without the needle. This effectively creates a scenario which is analogous to having two springs with different stiffnesses connected in series. When both sections are put under the same load, the strain on the uncovered FBG section will be larger. A qualitative representation of the axial strain along the length of the fiber is also show in Figure 3.5.

39

Creating these two sections along the length of the FBG with different stiffnesses allows the FBG to have two sections with different effective strain sensitivities. In other words, as load is applied to the anchors in Figure 3.5, the optical interrogator should record two distinct peaks that represent two distinct Bragg wavelengths. An example of a spectrum with peak splitting is shown in Figure 3.6.
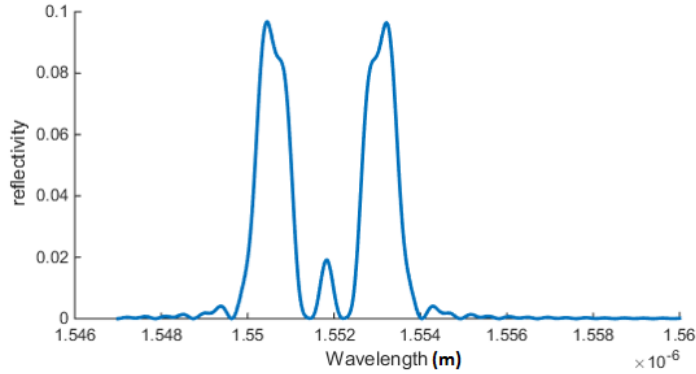
Figure 3.6: Example of peak splitting in a dual parameter FBG.

Equation 3.3 describes how the Bragg wavelength of a single FBG will change based on strain and temperature. If multiple FBGs are subject to the same strain/temperature mutiple bragg wavelengths can be recorded. Equation 3.19 show a matrix Equation relating the two Bragg wavelengths.

$$
\begin{bmatrix} \Delta\lambda_1 \\ \Delta\lambda_2 \end{bmatrix} = \begin{bmatrix} \gamma_1\Delta\epsilon + \phi_1\Delta T \\ \gamma_2\Delta\epsilon + \phi_2\Delta T \end{bmatrix} \tag{3.19}
$$

Since both FBGs are subject to the same temperature and strain changes, a sensitivity matrix $\mathbf{K}$ can be isolated.

40

$$
\begin{bmatrix} \Delta\lambda_1 \\ \Delta\lambda_2 \end{bmatrix} = \begin{bmatrix} \gamma_1 & \phi_1 \\ \gamma_2 & \phi_2 \end{bmatrix} \begin{bmatrix} \Delta\epsilon \\ \Delta T \end{bmatrix} \tag{3.20}
$$

$$
\boldsymbol{K} = \begin{bmatrix} \gamma_1 & \phi_1 \\ \gamma_2 & \phi_2 \end{bmatrix} \tag{3.21}
$$

As long as the columns of the sensitivity matrix $\mathbf{K}$ are linearly independent (i.e. rank($\mathbf{K}$)=2), the sensitivity matrix can be inverted and the strain/temperature state of the sensor can be determined from the two recorded Bragg wavelengths.

In other words, to produce a dual paramter sensor, two Bragg wavelength peaks with different sensitivities are recorded simultaneously.

Single Needle Embedded Dual Parameter Sensor

The first design of an EDPS was based on the design from [22] and on the embedding process for single parameter sensors developed in this thesis. As described in Sections 3.3.2 and 3.3.1, the embedding procedure consists of first drilling a hole in the host material, then using silver nanoparticle paste as an adhesive to bond the fiber to the host material. This embedding procedure can be used to embed a dual parameter sensor.

The design of the single needle EDPS is shown in Figure 3.7. The single needle EDPS is simply an embedded single parameter sensor with an additional needle around half the FBG. The needle was expected to produce two sections with different strain sensitivities along the length of the FBG, similarly to the single needle external dual parameter sensor.

To have a better understanding of the strain along the length of the FBG, Finite Element Analysis (FEA) was done to give a good estimation fiber axial strain. COMSOL
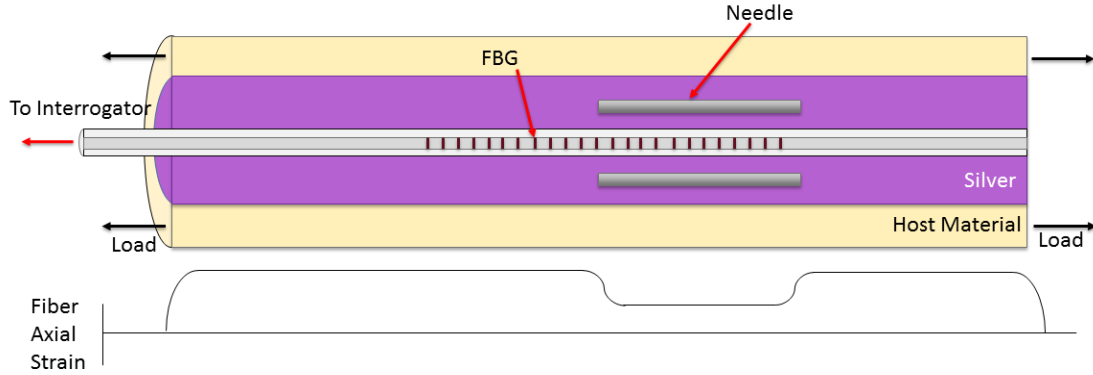
Figure 3.7: Single needle EDPS.

Multiphysics 4.4 was used as the main FEA software.

The material properties used in the FEA are outlined in Table 3.4. The dimensions of the components in the FEA are outlined in Table 3.5.

Table 3.4: Material properties used in FEA.

Material	Elastic Modulus(GPa)	Poisson's Ratio
Sintered Silver	15.0	0.37
Silica Glass	73.1	0.17
316 Stainless Steel	205	0.28
AZ31B Magnesium Alloy	45.0	0.29

The entire system was modelled as an axisymmetric model with the symmetric axis at the center of the fiber. All material was assumed to behave in an isotropic, linear elastic manner following Hooke's law and assuming infinitesimal strain.

Mesh independence analysis was done on all FEA results. The maximum element size used which allowed solution convergence was 30 μm. The MUMPS solver along with the

42

Table 3.5: Dimension of Components for FEA.

Dimension	Value	Unit
Total Length	15	mm
Total Diameter	10	mm
Fiber Diameter	125	μm
Needle Inner Diameter	184	μm
Needle Outer Diameter	336.4	μm
Needle Length	5	mm
Drilled Hole Diameter	700	μm

approximate minimum fill preordering algorithm was used. The host material (AZ31B) was put under 20, 40, and 60 MPa axial stress while the fiber and the silver were left unloaded, this loading condition is shown in Figure 3.7.

The strain transfer ratio from the FEA of the single needle EDPS is show in Figure 3.8. Strain transfer ratio is the ratio of the strain experienced by the fiber relative to the strain experienced by the host material. In Figure 3.8 the strain transfer ratio is plotted with respect to the length of the embedded portion of the fiber.

In Figure 3.8, the strain transfer ratio from 0 to 5 mm is very similar to the strain transfer ratio described in Figure 3.4. The first 2.5mm of embedded fiber are required to allow the silver to properly transfer strain to the fiber. The section from 2mm to 5mm has a strain transfer ratio of 1. This shows that the strain on the fiber between 2mm and 5mm perfectly matches the strain in the host material.

The section of fiber from 7.5mm to 12.5mm is surrounded by the stainless steel needle. As previously described, the purpose of the needle was to strengthen the section and to reduce the strain transfer ratio. The needle does not produce the same effect for an embedded sensor as for an external sensor. Near the ends of the needle (at 7.5mm and
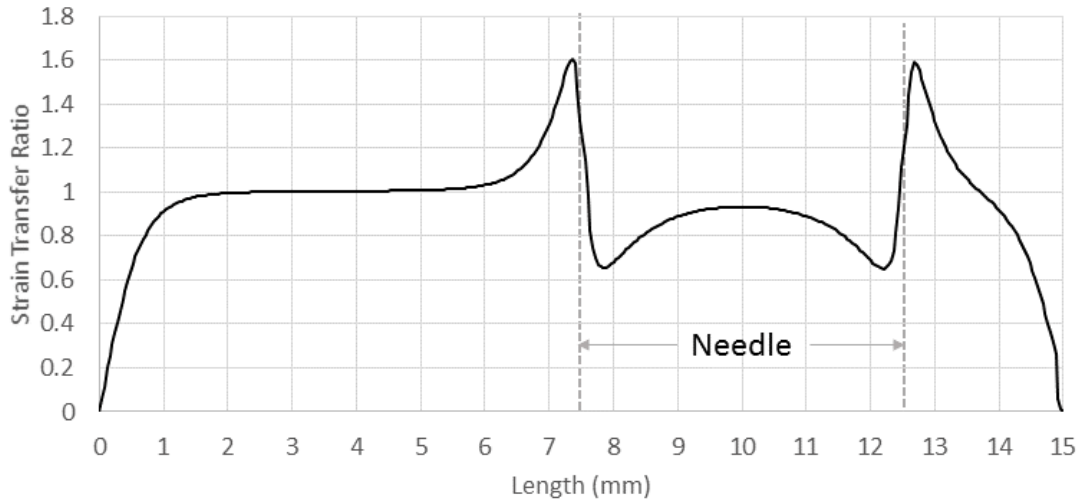
Figure 3.8: Strain transfer of a single needle EDPS from FEA.

12.5mm) there are large fluctuations in strain transfer ratio. Along the length of the needle (between 7.5mm and 12.5mm), the strain transfer ratio is not constant. This fluctuating, non-constant behaviour of the strain transfer ratio means that the fiber is not experiencing constant strain in this section.

The main cause of the strain-transfer ratio fluctuations along the needle section is the coupling of the strain from the host material to the needle. Although the needle does reinforce the section and it does reduce the strain transfer ratio near the ends of the needle, the strain transfer ratio still approaches a value of 1 near the center of the needle. If the needle were long enough, the strain transfer ratio at the center would reach 1. The behaviour can be described analytically using a similar model to the one outlined in Section 3.1.1.

All previous discussion on FEA results has only described the strain transfer along a plain fiber without Bragg grating. We will now consider that the embedded fiber has an

8mm Bragg grating starting at 3mm and ending at 11mm in Figure 3.8.

The first section of the FBG from 3mm to 5mm would experience a strain transfer ratio of 1. The second section of the FBG from 5mm to 11mm would experience a varying strain transfer ratio. This configuration should therefore produce a single strong peak in reflectivity and significant noisy side lobes around the peak.

To quantitatively examine the spectrum produced by this strain distribution along the fiber, the model from Section 3.1.3 and the Matlab implementation from Appendix A were used to produce an FBG spectrum.

The spectra produced using the Matlab model had a center wavelength of 1530 nm, a fringe visibility of 1, and a DC index change 10^{-4}. Each spectrum plot shows the predicted reflectivity spectrum of the FBG at 0.1, 0.3, and 0.5 percent strain at ambient temperature. Figure 3.9 shows the reflectivity spectrum for the single needle EDPS. Figures 3.12, 3.15, and 3.18 were produced using the same parameters as the spectrum in Figure 3.9.
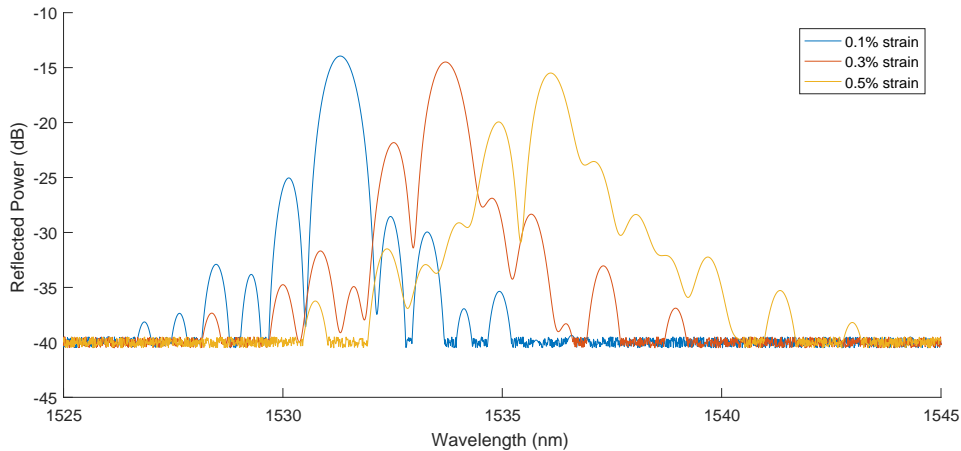
Figure 3.9: Reflectivity spectrum of single needle EDPS.

As expected, there is only one discernible peak and significant side lobe noise for all simulated strains in Figure 3.9. Two clearly detectable peaks with differing sensitivities

45

are necessary to be able to determine the strain-temperature state of the system using Equation 3.20. The single needle EDPS was not constructed due to this result.

Double Needle Embedded Dual Parameter Sensor

The main issue with the single needle EDPS was the strain transfer of the host material to the fiber through the needle. The double needle EDPS design attempted to eliminate the shear strain transfer through the needle.

To eliminate the undesirable strain transfer effects, an outer needle was added to the design of the EDPS as shown in Figure 3.10. Essentially, the double needle EDPS is a single needle external dual parameter sensor encased in a protective outer needle. The main purpose of the outer needle is to prevent the silver adhesive from bonding to the FBG and the inner needle by creating an interlayer of air between the inner and outer needle.
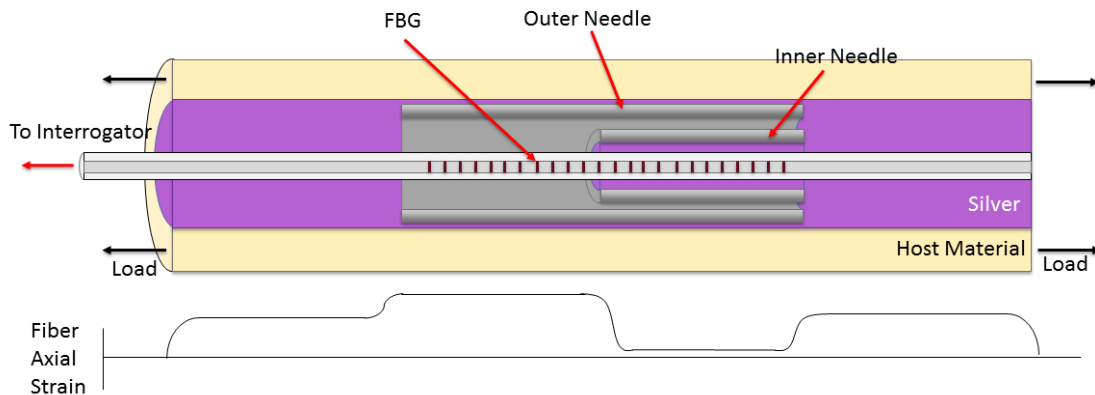
Figure 3.10: Double needle EDPS.

The air interlayer eliminates any strain transfer from the host material to the FBG through shear. All strain is axially transfered to the FBG from the ends of the fiber that

are bonded to the silver adhesive beyond of the outer needle.

To determine strain distribution along the length of the double needle EDPS, FEA was done. All material parameters for the FEA were taken from Table 3.4. Dimensions were taken from Table 3.5 with the addition of a 10 mm long, 22 gauge needle (717.6 μm OD, 413 μm ID). All other FEA parameters and procedures were identical to those in Section 3.3.3. The result of the FEA is shown in Figure 3.11.
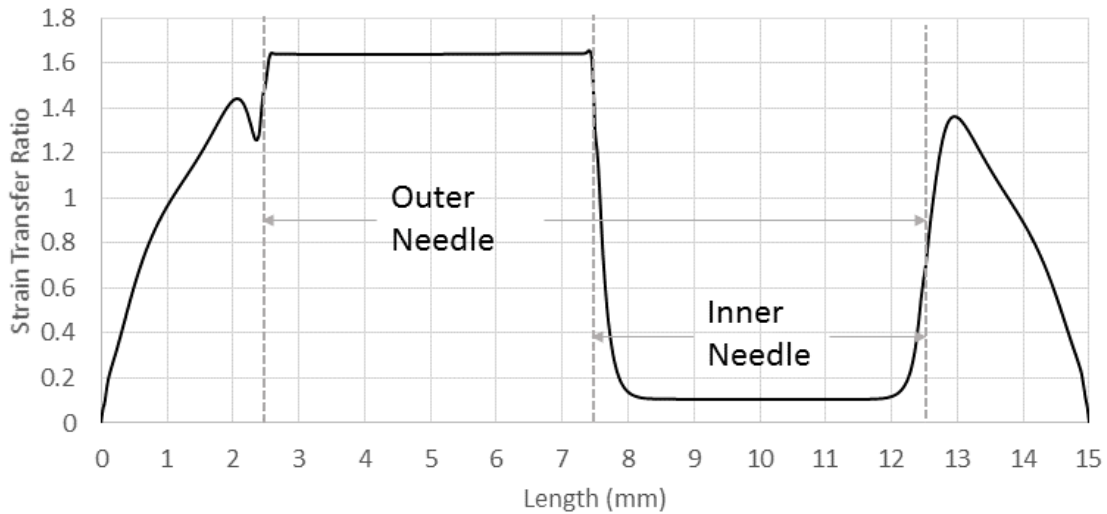
Figure 3.11: Strain transfer of a Double needle EDPS from FEA.

The double needle design produces two regions with different strain transfer ratios. The uncovered section of FBG experiences a strain transfer ratio of 1.6. This large strain transfer ratio means that the uncovered section of the FBG should be more sensitive to strain than than the covered section which experiences a strain transfer ratio of 0.1. This result shows that the air interlayer successfully eliminates the undesirable strain effects that were present in the single needle EDPS.

The transition section between the uncovered section and the covered section of the

47

FBG is limited to 0.6mm of the fiber length. If a sufficient fraction of the FBG is experiencing constant strain in either the covered or uncovered section, the resulting spectrum should have limited side lobe noise.

We will now consider that an FBG is placed from 3mm to 11mm along the length of the fiber from Figure 3.11. The optomechanical model from Appendix A was used to produce a reflectivity spectrum for the double needle EDPS. The reflectivity spectrum is shown in Figure 3.12.
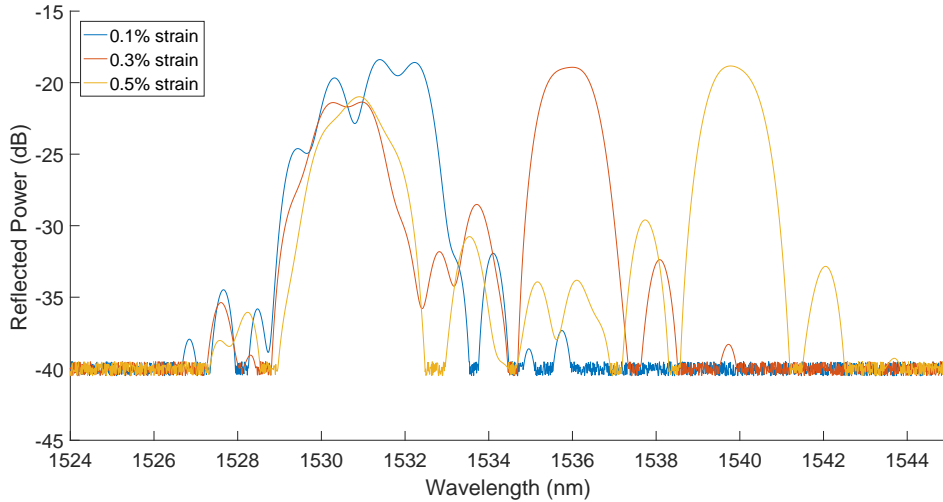
Figure 3.12: Reflectivity spectrum of double needle EDPS.

The spectra in Figure 3.12 show two clear peaks forming with increasing strain. The presence of two clearly identifiable peaks shows that this FBG configuration may be used as dual parameter sensor at higher strain. At 0.1% strain, however, two peaks cannot be clearly identified and determination of the strain-temperature state may be difficult.

A prototype of the double needle EDPS was constructed due to the promising results from the FEA and optomechanical modeling. All materials and dimensions were identical to those used in section 3.3.3 and in Tables 3.4 and 3.5. The embedding procedure was

identical to the procedure described in Section 3.3.2 with the addition of both inner and outer needles. The needles were first positioned, silver paste was then applied to the appropriate areas of the double needle EDPS.

Although analytical and numerical modeling of the double needle EDPS design showed promising results, the double needle design was found to have two major flaws. Due to the small size of the inner needle and the high viscosity of the silver paste, reliably depositing silver paste between the inner needle and the fiber was extremely difficult. Additionally, manipulation of multiple needles and maintaining then air interlayer before sintering was challenging. Despite the impractical assembly procedure, several prototypes were successfully assembled and sintering was attempted.

The sintering of the double needle EDPS's demonstrated another major flaw in their design. After the sintering of the prototype was complete, the EDPS was allowed to cool to ambient temperature. During the cooldown phase, all 6 double needle EDPS prototypes failed suddenly and all reflectivity peaks disappeared. The cause of the sudden loss of signal during cooldown was attributed to the difference in the coefficient of thermal expansion between the glass fiber and metallic host material.

During the sintering stage of the embedding process, the entire host part, fiber, needles, and silver is heated to $260°C$ before bonding occurs. AZ31B has a coefficient of thermal expansion 26 $\mu m/m°C$ while fused silica glass fibers has a coefficient of thermal expansion of 0.54 $\mu m/m°C$ [54]. Once the sintering is complete, the fiber should be under relatively little strain, however, as the metallic host part cools down it will experience significantly more compressive strain than the glass fiber due to their differing coefficients of thermal expansion. Sections of the glass fiber are not supported by any material in the double EDPS and can therefore be prone to buckling and fracture if excessive mechanical compressive strains are applied to the fiber by the host material. Buckling of the unsupported fiber

49

due to differing coefficients of thermal expansion was presumed to be main failure mode.

Single Needle Floating End Embedded Dual Parameter Sensor

The lessons learned from previous EDPS designs were taken into account and a list of design requirements was formulated to guide a new design for an EDPS.

The critical design requirements are as follows:

- There must be two FBG sections with different but constant strain transfer ratios to produce two clear peaks in the reflectivity spectrum

- The transition region between the FBG sections with different strain transfer ratios should be small to avoid noise in the produced reflectivity spectrum

- To avoid fiber buckling, there should be no unsupported sections of fiber that can be exposed to compressive strain

- To simplify assembly, the number of needles should be minimized and no silver should be placed between a needle and the fiber

With these new criteria, the single needle, floating end EDPS was designed. This design will be referred as the "floating EDPS" for simplicity. Figure 3.13 shows a diagram of the floating EDPS.

The design of the floating EDPS only contains a single needle and no silver is placed between a needle and the fiber. This simplified design allows for easier assembly during the embedding process. A section of fiber is protected by a needle to allow a air interlayer between the fiber and the host material. The fiber terminates inside the needle to create
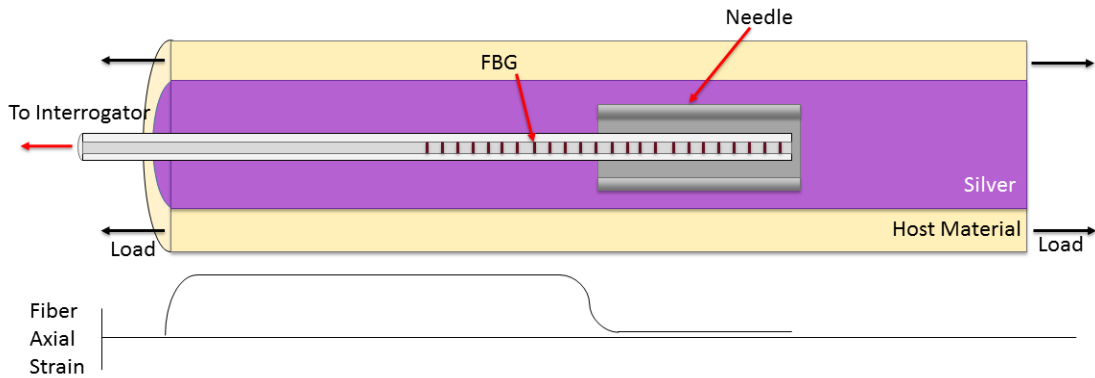
Figure 3.13: Single needle floating end EDPS.

the so called "floating" end of the fiber. The floating end should have a strain transfer
ratio of zero because it is not connected to the host material.
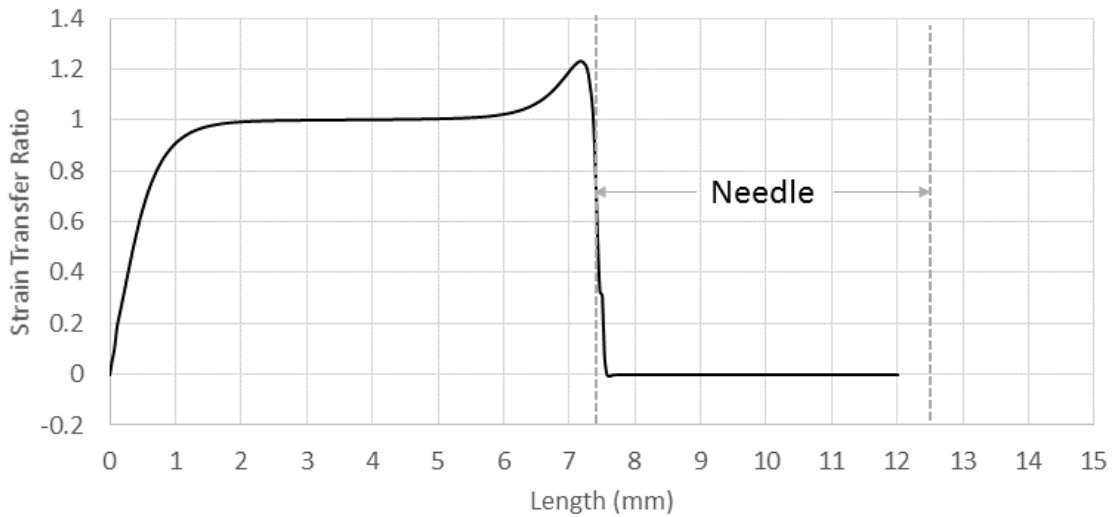
Figure 3.14: Strain transfer of a single needle floating end EDPS from FEA.

FEA was performed to determine the strain transfer ratio along the length of the fiber
for the floating EDPS. All material parameters for the FEA were taken from Table 3.4.
Dimensions were taken from Table 3.5 with the fiber prematurely terminated 0.5 mm before

51

the end of the needle. All other FEA parameters and procedures were identical to those done in Section 3.3.3. The result of the FEA is shown in Figure 3.14.

As expected, the FEA indicates that the floating end of the fiber exhibits a strain transfer ratio of 0. The bonded section of the fiber has a strain transfer ratio of 1 between 2mm and 5mm. There is a transition section of non-constant strain transfer between 6mm and 7.5mm. To effectively capture the strain at both the floating section and the bonded section, a FBG was assumed to be placed from 3mm to 11mm. The reflectivity spectrum resulting from this FBG was determined using the optomechanical model described in Appendix A along with the same optical parameters as described in Section 3.3.3. The spectrum for the floating end EPDS is shown in Figure 3.15.
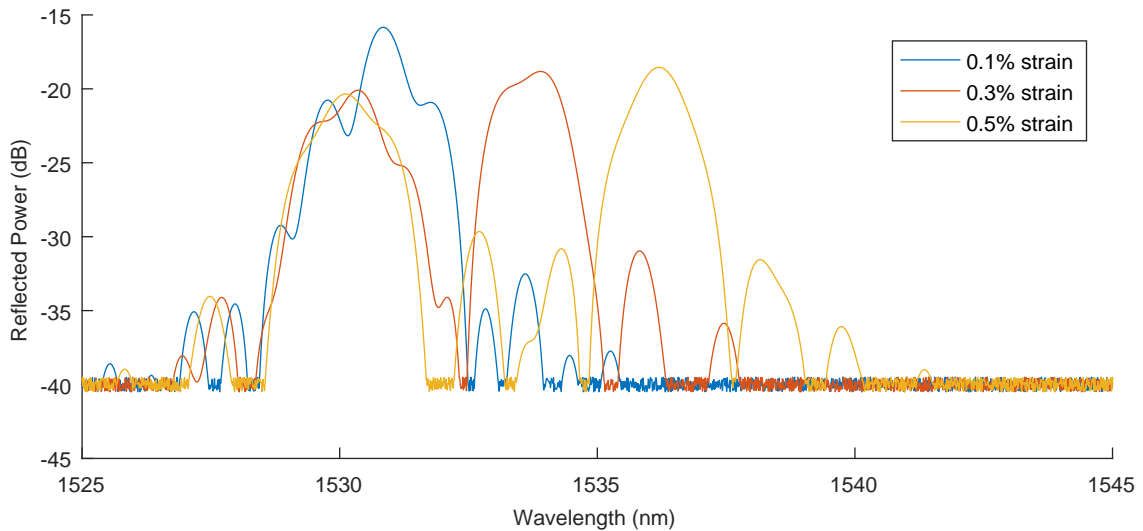
Figure 3.15: Reflectivity spectrum of single needle floating end EDPS from model.

The appearance of two clear Bragg wavelength peaks can be seen in Figure 3.15 at 0.3% and 0.5% strain. These peaks along with Equation 3.20 can be used to determine the strain-temperature state of the sensor. At 0.1% strain, two peaks are not clearly visible and there is some side lobe noise likely cause by the transition section of the floating end

EDPS. This noise and the lack of two peaks at low strain may cause problems when trying to determine the strain-temperature state of the sensor.

A prototype of the floating needle EDPS was constructed using the same materials and dimensions used in the FEA and the optomechanical model of the floating needle EDPS. The embedding procedure was identical to the one described in 3.3.2 with the addition of the single needle. The floating needle EDPS assembly was simple and more practical than the double needle EDPS assembly. There was no loss of signal during the sintering process or during the cooldown of the sensor. Due to the difference in the coefficients of thermal expansion between glass and AZ31B, a comnpressive strain of -0.6% was expected. This compressive strain created during cooldown should result in the creation of two clear Bragg wavelength peaks at room temperature. The actual reflectivity spectrum of the floating end EDPS is shown in Figure 3.16.
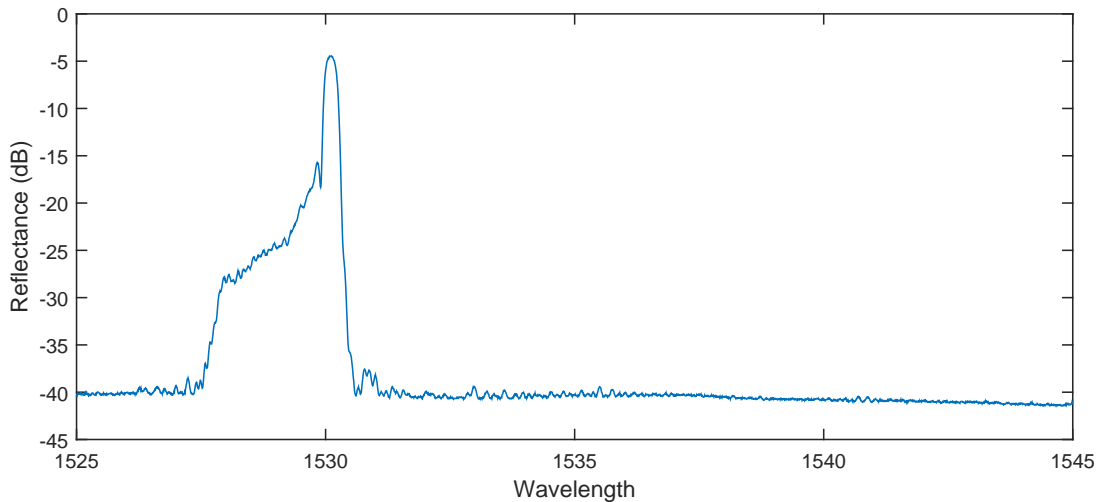
Figure 3.16: Reflectivity spectrum of single needle floating end EDPS prototype.

Only a single peak is identifiable in Figure 3.16. A noticeable plateau beside the peak can also be identified. The single peak is produced by the floating end of the FBG and

the plateau is likely cause by the bonded section of the FBG. A plateau of this kind may be caused by a very large transition period which has non-constant strain transfer. This non-constant strain can spread out the second Bragg wavelength peak and turn it into a plateau rather than a clear peak. In the FEA and the optomechanical model, perfect bonding is assumed between the fiber and silver. In practice, the transition region may be larger due to imperfect bonding. Imperfect bonding and an increased transition region of non-constant strain transfer was presumed to be the cause of the plateau. Several floating EDPS prototypes were constructed with similar results.

To eliminate the plateauing of the second Bragg wavelength peak, the floating EDPS was modified to have two distinct gratings on the fiber. Figure 3.17 shows the design of the modified floating EDPS.
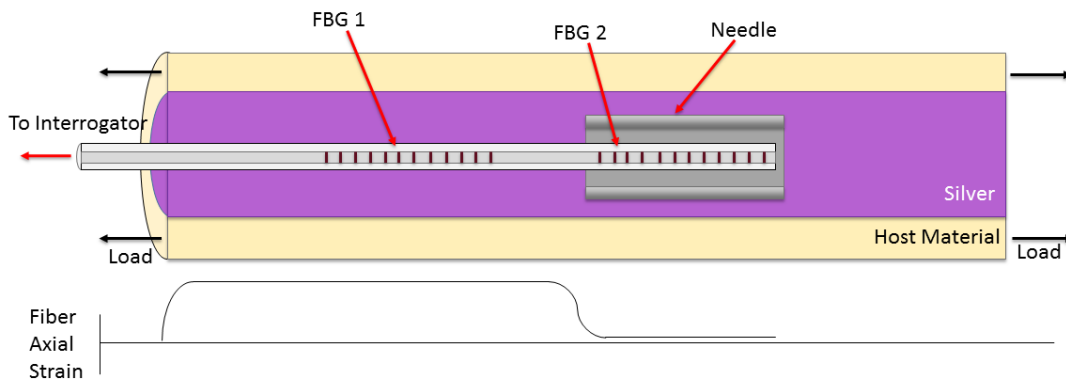
Figure 3.17: Modified single needle floating end EDPS.

Since the geometry of the sensor has not changed, the strain transfer of the modified floating EDPS can be described by Figure 3.14. The modified floating EDPS has grating sections from 2.5mm to 5mm and from 8mm to 11mm rather than a single uniform grating. The resulting spectrum from the optomechanical model is shown in Figure 3.18.

The clear difference between Figure 3.18 and Figure 3.15 is the less noisy peaks at lower

54
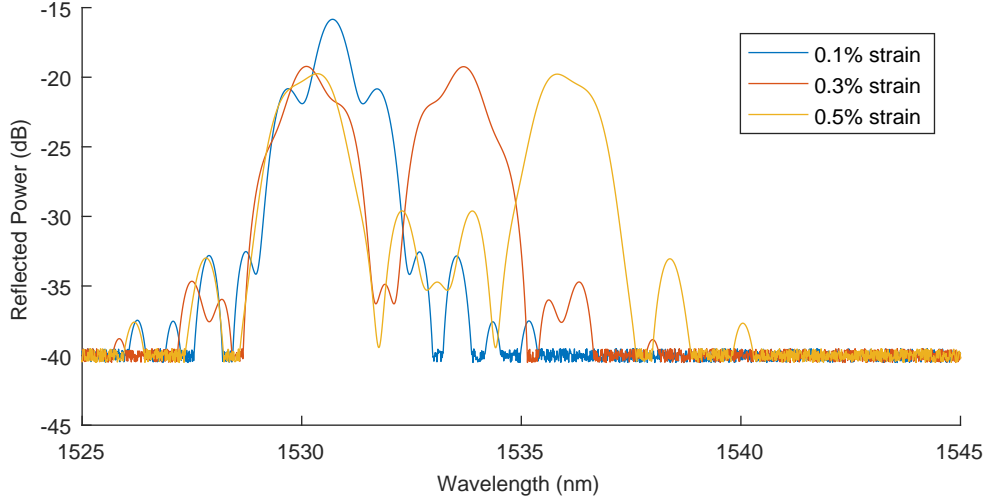
Figure 3.18: Reflectivity spectrum of modified single needle floating end EDPS.

strain. The lower noise could allow for better strain-temperature determination at lower strains.

A single prototype of the modified floating EDPS was constructed. Due to time constraints and material constraints, two 10mm grating on separate fibers were embedded in a single sample rather than two grating on a single fiber. The distinct gratings were coupled using a Thorlabs 4x1 fiber coupler. The resulting spectrum of the modified floating EDPS is shown in Figure 3.19. This spectrum was recorded at ambient temperature under zero external strain.

Two clear Bragg wavelength peaks can be seen in Figure 3.19. The peak splitting at room temperature under zero strain is consistent with the compressive strain caused during the cooldown stage of the sintering process.

The sensitivity of both FBGs in the floating EDPS can be calculated using the simplified optomechanical model in Section 3.1.2. We will presume the two following conditions:
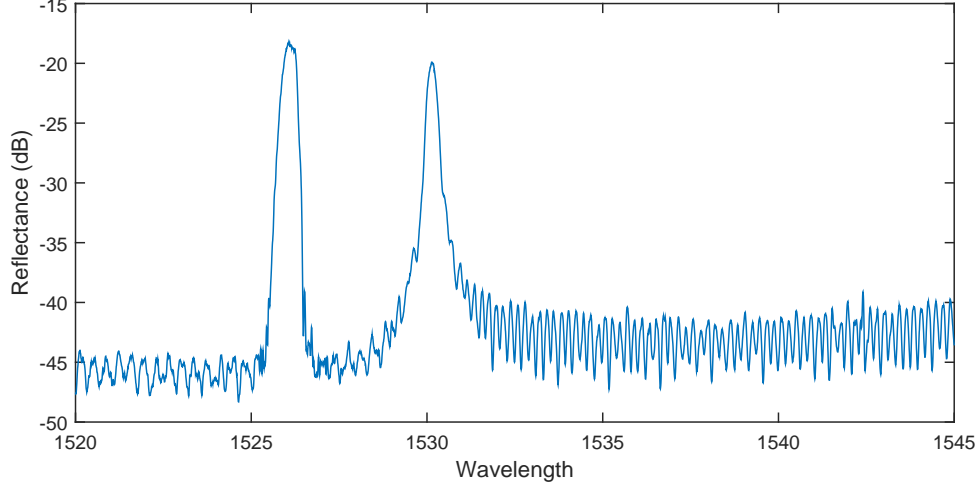
Figure 3.19: Reflectivity spectrum of modified single needle floating end EDPS prototype.

- The floating FBG has a strain transfer ratio of 0

- The embedded FBG has a strain transfer ratio of 1

Equation 3.7 is valid for the embedded FBG, however, Equation 3.7 must be modified for the floating FBG. Since the strain transfer ratio is 0, the FBG should experience no strain from the host material. The wavelength-strain coefficient γ should therefore be zero. The floating FBG should also experience thermal strain based on the thermal expansion coefficient of fused silica rather than the thermal expansion coefficient of the host material. Equation 3.22 takes into account these facts and can be used to predict the shift in Bragg wavelength of the floating FBG.

$$\Delta\lambda_B = \lambda_0 \left(\frac{1}{n_{eff}} \left(\frac{dn}{dt} \right) + \alpha_f (1 - p_e) \right) \Delta T \tag{3.22}$$

Using Equations 3.7 and 3.22 along with the material parameters in Table 3.1, the strain and temperature sensitivities of both FBGs can be predicted. Table 3.6 gives the

predicted sensitivities of the floating FBG and the embedded FBG in the floating EDPS.

Table 3.6: Expected sensitivity of floating EDPS.

	Strain Sensitivity	Temperature Sensitivity
Embedded FBG	1.19 pm/$\mu\epsilon$	42.7 pm/°C
Floating FBG	0 pm/$\mu\epsilon$	11.7 pm/°C

The sensitivities in Table 3.6 can be used to complete the sensitivity matrix described in Equation 3.21 and can be used to convert the two Bragg wavelengths produced by the floating EDPS into the full temperature-strain state of the sensor.

The performance of the successful prototype of the modified floating EDPS is examined in Section 4.2.

3.4 Summary

Three models were developped in this Chapter. The first model describes how strain from a host material is transfered to an embedded fiber. The second model describes how the Bragg wavelength of an embedded FBG is affected by either strain or temperature changes of the host material. The third model can be used to produce a reflectivity spectrum of an embedded FBG that is subject to non-uniform strain.

The embedding procedure was described in the section along with the material properties of the host material, the fiber, and the adhesive.

The design of single and dual-parameter sensors were also examined in this Chapter. Three specific dual-parameter sensor designes were examined in detail. The performance of these designs was examined using the models developed in this thesis along with FEA.

Chapter 4

Experimental Validation

In the previous chapter, a procedure to embed optical fibers into metallic structures was described along with the design of both single and dual-parameter sensors. In this chapter, the performance of embedded single-parameter and dual-parameter sensors are determined experimentally. A total of 22 single-parameter sensors were subject to tensile testing and repeatability testing. One prototype of an embedded dual-parameter sensor was subject to a temperature and a tensile test.

The primary goal of all experiments described in this chapter was to determine the viability of both the silver nanoparticle embedding process and the design for single and dual parameter sensors. The scope of the experimental work was only wide enough for technology validation and not for thorough performance characterization.

The equipment used, the testing procedures, and the experimental results are all discussed in this chapter.

4.1 Single Parameter Sensor Testing

4.1.1 Testing Equipment

Both tensile tests and repeatability tests used the same testing equipment. An Instron model 1331 was used as a tensile machine along with a enclosure furnace for temperature control. FBG data aquisition was done using a Micron Optics sm125-200 optical interrogator. Temperature data acquisition was done with a National Instrument NI-9162 Thermocouple DAQ and a K-type thermocouple. The strain on the sample was recorded using a Digital Image Correlation (DIC) system build by GOM. The general arrangement of all the measurement equipment is shown in Figure 4.1.
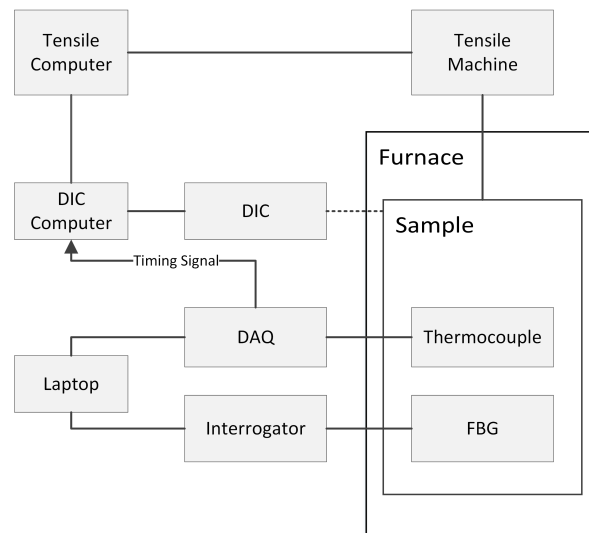
Figure 4.1: Testing equipment used during tensile and repeatibility test.

All single parameter test samples used AZ31B-H24 as a host material. A channel was machined at the surface of the magnesium test sample prior to embedding. The geometry of the test samples is described in Appendix B. Uniform 10mm long FBGs with properties

described in Table 3.1 were used. The procedure used to embed the single parameter FBGs is described in Section 3.3.2.

The magnesium tensile sample was placed in the grippers of the tensile machine and the thermocouple was subsequently fixed to the surface of the sample. The DIC cameras captured images of the sample through the window of the furnace.

The strain signal from the DIC and the temperature signal from the thermocouple served as reference signals. All measurements from the FBG sensor were compared to these reference signals.

4.1.2 Tensile Test Procedure

The purpose of the tensile tests was to determine the maximum strain of the sensors over a range of temperatures. The strain sensitivity of the FBG was also determined from the tensile tests

The following procedure was followed for the tensile tests:

1. The sample was placed in the tensile machine. The thermocouple was adhered to the surface of the sample.

2. The furnace was closed and heated to the setpoint temperature. The temperature of the sample was allowed to reach steady state (roughly 30 minutes). The sample was kept under zero load during the heating process.

3. The sample was then loaded in tension with an extension of 1.5 mm/min until failure of the FBG sensor.

The tensile test was performed at 3 setpoint temperatures. 6 samples were tested at 25°C, 6 samples were tested at 150°C, and 5 samples were tested at 350°C for a total of 17 tensile tests.
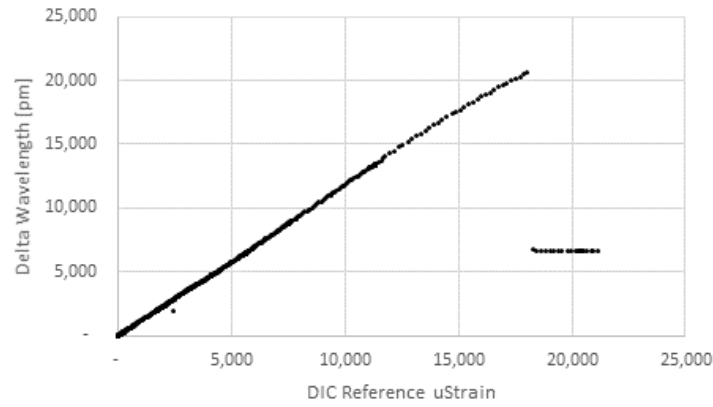
4.1.3 Tensile Test Results

During the single-parameter tensile tests, 3 critical parameters are recorded simultaneously: the temperature of the sample, the strain on the sample, and the Bragg wavelength of the FBG. For all the single-parameter tensile tests, the temperature is kept constant while the strain on the sample increases. The main goal of this test was to examine the correlation between strain and Bragg wavelength at several different temperatures.

Figure 4.2 shows the shift in the measured Bragg wavelength as a function of the reference strain measured by the DIC for two of the samples tested at room temperature. One critical characteristic of the embedded sensors is the linear relationship between the Bragg wavelength and the strain on the sample. Once the linear relationship no longer holds, the sensor is considered to have failed. Figure 4.2a shows a clear example of an adhesive failure during the tensile test. As the strain on the sample exceeds 18,000 $\mu\epsilon$ (or 1.8%), the wavelength signal loses all correlation to the strain on the sample. Figure 4.2b shows an example of a fiber failure. The sudden loss of wavelength signal before adhesive failure is consistent with a break in the fiber in the sample. All tensile tests had either a fiber failure or adhesive failure similar to what is shown in Figure 3.2.

The sensitivity of an FBG to strain can be found by looking at the slope of the linear section in wavelength/strain plots like the ones in Figure 4.2. All strain-sensitivity values for embedded single parameter sensors were determined by using linear least-square fitting on wavelength/strain data from the start of the test up until the failure of the sensor (either
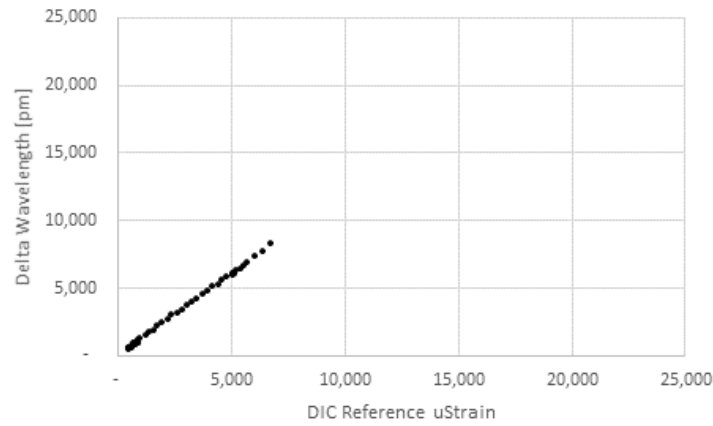
Figure 4.2: Wavelength shift vs DIC strain of a) sample 1 at 25° b) sample 2 at 25°.

fiber failure or adhesive failure). The slope of trendline is used as the FBG's sensitivity.

Figure 4.3 shows the aggregated results of all the tensile tests on the embedded single parameter FBG sensor samples. Figure 4.3a shows the maximum strain of the samples as a function of temperature. The maximum strain was defined as the point at which either bond failure or fiber failure occurs. It is important to note that the strain in Figure 4.3a is only the load induced strain, the strain induced by thermal expansion of the host

material is additional. The maximum strain appears to decrease as sample temperature increases, however, the standard deviation of the maximum strain values is significant at all temperatures. All samples were produced manually and each individual sample may have had inconsistent hidden defects in the silver adhesive layer. This sample inconsistency may account for the large standard deviation of maximum strain.
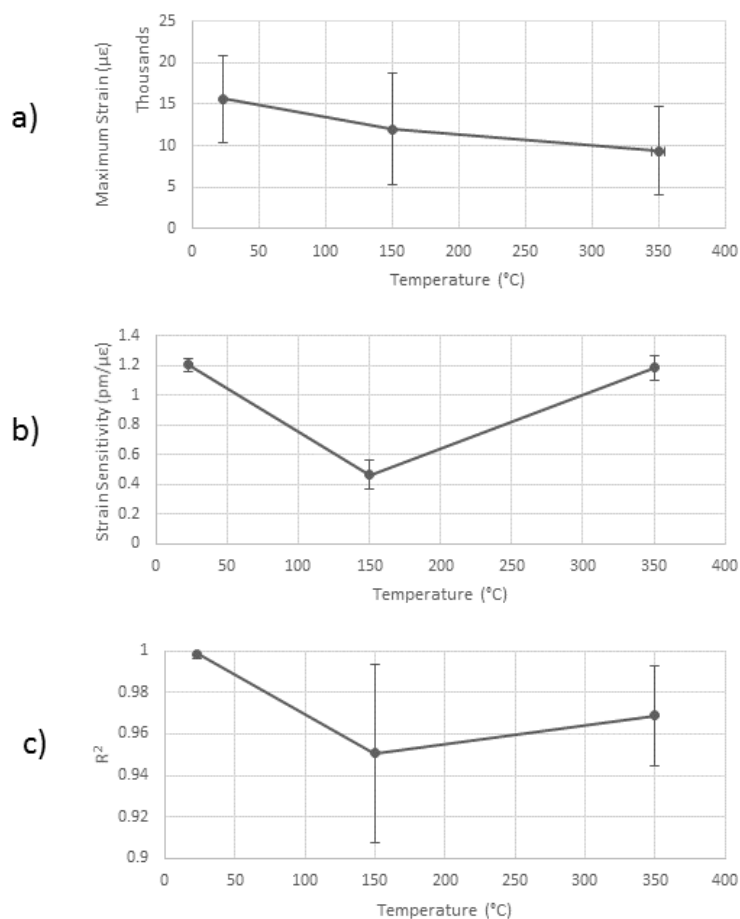

Figure 4.3: Embedded single parameter FBG sensor a) maximum strain, b) strain sensitivity 25°, and c) R^2 vs temperature

Figure 4.3b shows the strain sensitivity of the samples as a function of the sample

temperature. Table 3.3 describes the expected strain sensitivity to be 1.2 pm/$\mu\epsilon$. The mean temperature sensitivity of the embedded sensors is 1.2 pm/$\mu\epsilon$ for the 25° and 350° samples. The mean strain sensitivity of the 150° samples is 0.47pm/$\mu\epsilon$. The recorded strain sensitivity at room temperature and at 350° agrees with the expected sensitivity, however at 150°, there is a clear discrepancy between the recorded and the expected sensitivity. The reason for the decrease in strain sensitivity at 150° is unclear, the tensile tests would need to be repeated to confirm the results and eliminate the possibility of a data recording error.

Figure 4.3c shows the coefficient of determination (R^2) for a least square linear regression between the shift in Bragg wavelength and the DIC strain. The R^2 value can be used as a metric for determining any deviations from linearity. At room temperature, the embedded fibers the wavelength-strain relationship is highly linear with an R^2 value of 0.998. With increasing temperature, the R^2 value decreases. The decrease in linearity with increasing temperature was partially caused by the introduction of heat shimmer noise captured by the DIC system cameras. The cleanliness of the glass window on the furnace may have also affected the DIC signal. The departure from linearity at higher temperature may be also be caused by slow failure of the bonding layer at higher temperature. To confirm any of these possible noise sources, more tests with different reference strain sensing equipment would be required.

Figure 4.4 shows the failure mode of the embedded sensors. It is clear that at 23° and 150° the dominant failure mode is bond failure. At 350° the dominant failure mode is fiber failure. The bond failure at low temperature may have been caused by incomplete sintering or may be caused by increased ductility of the silver at high temperature. In future tests, a longer sintering procedure with higher sintering temperature may improve performance.
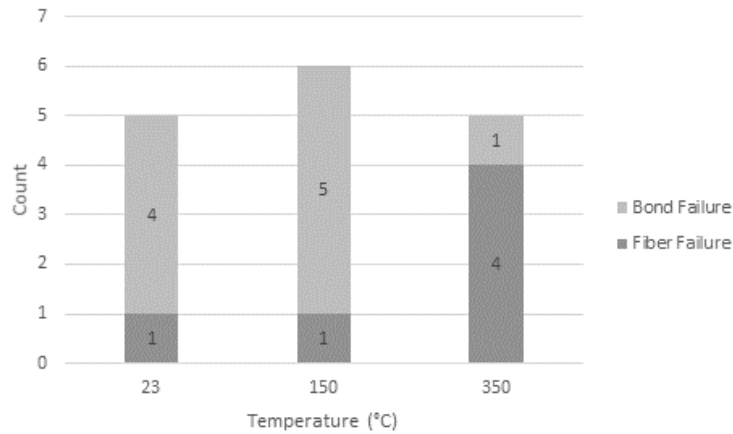
Figure 4.4: Failure mode of embedded single parameter FBGs.

4.1.4 Repeatability Test Procedure

The purpose of the repeatability tests was to examine the performance of the embedded FBG sensors under repeated loading and unloading cycles. The strain sensitivity and the temperature sensitivity was examined as a function of loading and temperature cycles.

The following procedure was followed for the repeatability tests:

1. The sample was placed in the tensile machine. The thermocouple was adhered to the surface of the sample.

2. The furnace was closed but left at ambient temperature.

3. The sample was then put under 1000 $\mu\epsilon$ in 200 $\mu\epsilon$ steps. The sample was then brought back to 0 $\mu\epsilon$ in 200 $\mu\epsilon$ steps.

4. The sample was heated to 150°C and allowed to reach steady state while under no load.

5. Step 3 was repeated.

6. The sample was heated to 350°C and allowed to reach steady state while under no load.

7. Step 3 was repeated.

8. The sample was allowed to return to room temperature.

9. Steps 3-8 were repeated two more times.

A total of 5 samples were run through the repeatability test. The first 3 samples failed before reaching step 7 of the cycle. For samples 4 and 5, the temperature at step 6 was reduced to 250°C.

4.1.5 Repeatability Test Results

The results of the repeatability tests can be separated into temperature sensitivity performance and strain sensitivity performance.

Strain Sensitivity Performance

This subsection looks at how the strain sensitivity of the embedded single-parameter sensors is affected by repeated changes in temperature and repeated loading cycles.

Figure 4.5a shows how the strain sensitivity changes based on the number of tensile loading steps. Each 'strain step' is equivalent to one run of step 3 in the repeatability test procedure. The R^2 value for each linear regression used to determine sensitivity is
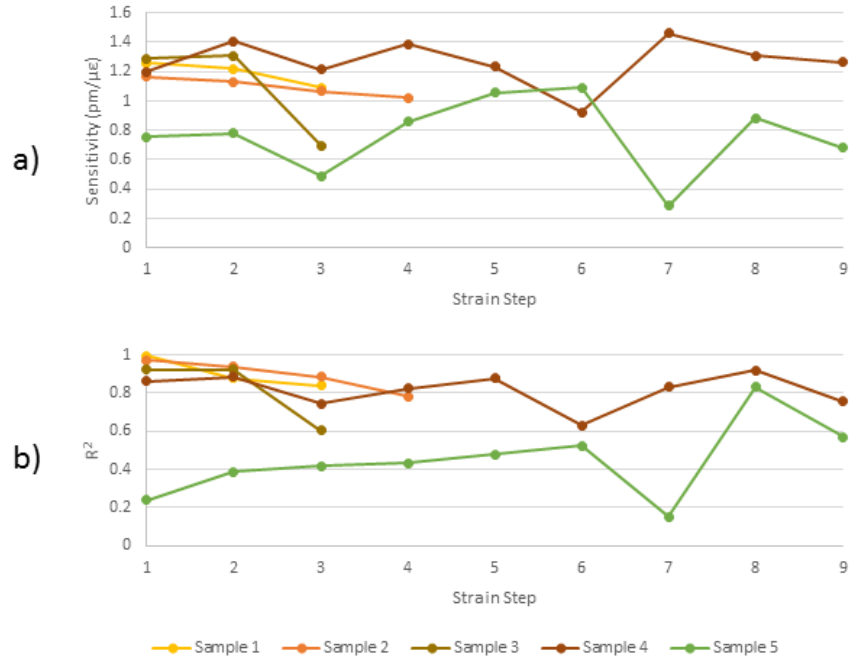
Figure 4.5: a)Strain sensitivity and b) R^2 vs cycle step.

also shown in 4.5b. Note that samples 1 to 3 fail before sample 4 and 5. The Maximum temperature for the repeatability tests was reduced to 250°C in samples 4 and 5.

The R^2 value for sample 5 shown in Figure 4.5 is significantly lower than the R^2 value for samples 1-4. Sample 5's low R^2 value was the result of a particularly poor DIC signal caused by improper focus in the cameras. Sample 5 will be considered an outlier and the strain data will be ignored.

Table 3.3 states that the predicted strain sensitivity for the embedded FBG sensor is 1.2 pm/$\mu\epsilon$. The sensitivity values of samples 1 to 4 seem to roughly agree with Table 3.3, although the sensitivity of sample 4 fluctuates significantly between strain steps. It is unclear if the fluctuation are caused by poor FBG performance or poor DIC signal. The sensitivity of sample 4 does not seem to drift with repeated tensile cycles, however, more

67

data with a less noisy reference strain source would be needed to definitively confirm this result.

Figure 4.6a shows how the strain sensitivity changes with changing temperature. Figure 4.6a shows the corresponding R^2 value. This Figure only includes samples 1 to 4 due to the poor R^2 value of sample 5.
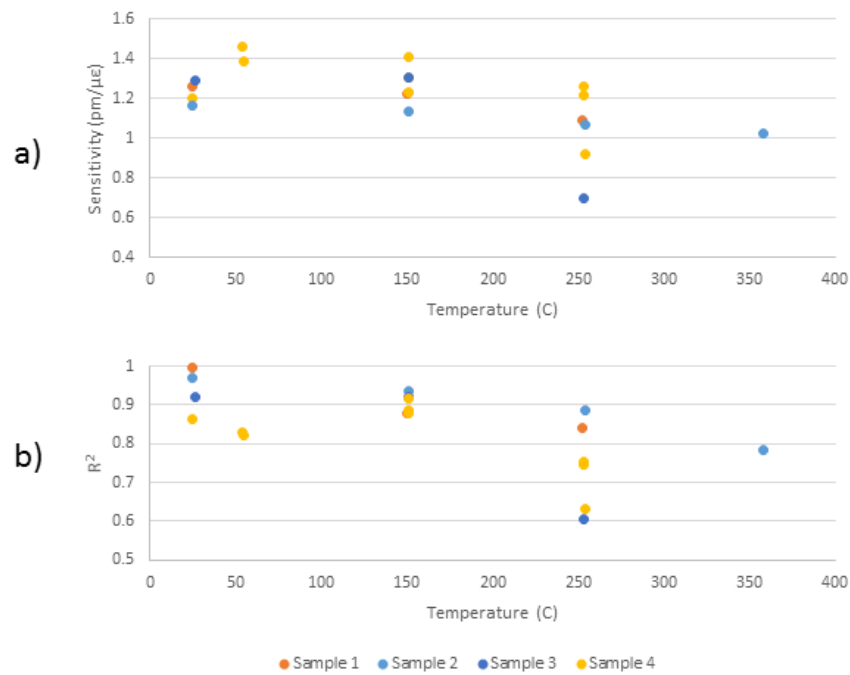
Figure 4.6: a)Strain sensitivity and b) R^2 vs temperature.

At 25°C and 150°C, the R^2 value seems to be roughly 0.9 for most samples while at 250°C, the R^2 value for samples range from 0.6 to 0.9. At 25°C and 150°C, the strain sensitivity is between 1 and 1.5 $pm/\mu\epsilon$. At 250°C, the strain sensitivity is between 0.6 and 1.3 $pm/\mu\epsilon$. The sensitivity values are generally around the expected $1.2pm/\mu\epsilon$, however, due to the low R^2 value, limited conclusions can be drawn from these data.

Temperature Sensitivity Performance

This subsection will look at how the temperature sensitivity of the embedded single-parameter sensors was affected by repeated temperature and strain cycles.

Figure 4.7 shows the temperature sensitivity and the R^2 value of the embedded single parameter sensors for repeated temperature steps. A 'temperature step' corresponds to either step 4, 6, or 8 of the testing procedure. These the loading on the sample was kept near zero during these temperature steps by manually jogging the jaw position of the tensile machine. This was a poor method for keeping the load at zero and likely introduced some non-linearity in the wavelength/temperature signal.

Figure 4.7: a)Temperature sensitivity and b) R^2 vs cycle step.

In Figure 4.7b, the R^2 value for all temperature steps was above 0.8 and was above 0.9 for most steps. During several steps, the thermocouple detached from the sample due

to the convection in the furnace. The R^2 value was below 0.9 due to the thermocouple reading the furnace air temperature rather than the sample surface temperature.

Table 3.3 states that the expected temperature sensitivity of the embedded single-parameter sensors should be $42.7pm/^\circ C$. In Figure 4.7b, samples 4 and 5 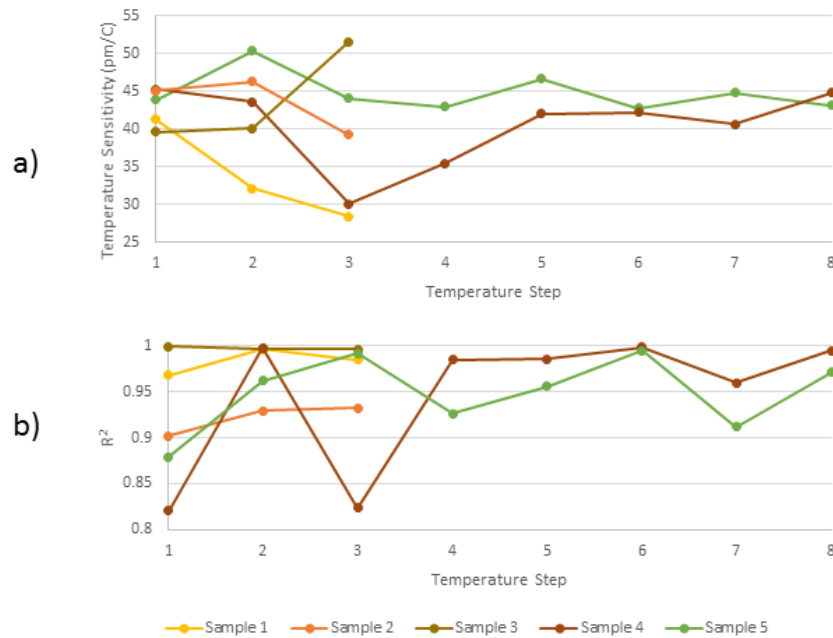seem to have relatively high R^2 values after temperature step 4. The corresponding temperature sensitivity of samples 4 and 5 after step 4 seems to reside between 40 and 46 $pm/^\circ C$. The recorded temperature sensitivity of the embedded single parameter sensors seems to stay near the expected temperature sensitivity even with repeated temperature cycles, although more tests with better R^2 are required to confirm these results.

4.2 Dual Parameter Sensor Testing

Due to time and material constraints only a single functioning embedded dual-parameter sensor prototype was assembled. The sensor design was a "single needle, floating end dual parameter sensor", this design is outlined in Section 3.3.3. A slight modification of the design was introduced due to availability of FBGs. Two discrete fibers with gratings were used instead of a single fiber with two gratings. The sensors were embedded in a AZ31B-H24 sample with a square channel machined at the surface. The geometry of the sample is described in Appendix B.

The dual parameter sensors were not tested as thoroughly as the single parameter sensors. The experimental results of this section are therefore more useful to prove the viability of the sensor package design rather than fully characterizing it's performance.

Only two tests were done on a single dual parameter sensor sample: a temperature test and a tensile test.

The temperature test consisted of a stepped increase in temperature from 20°C to 150 °C. The purpose of this test was to examine both Bragg wavelengths from the dual parameter sensor and to determine the sensitivity of each peak to temperature changes.

The tensile test consisted of a room temperature pull test using a manually operated desktop tensile machine. The strain on the sample was recorded using a surface mounted strain gauge and the resulting strain sensitivity of the Bragg wavelengths was determined.

4.2.1   Testing Equipment

Two different setups were used for the dual parameter sensor testing. The equipment used for these tests is outlined in Table 4.1.

Table 4.1: Equipment list for dual parameter sensor testing.

Equipment	Model
Manual Hand Test Stand	Shimana SHPMTS209
Force Gauge	Shimana SHPMFG177-1000N
Programmable Hot Plate	Torrey Pines HP40
Strain Gauge DAQ	National Instrument NI-9237
Strain Gauge	OMEGA KFH-3-350
Thermocouple DAQ	National Instrument NI-9211
Thermocouple	OMEGA Type T

The temperature tests used a programmable hot plate along with aluminum foil and fibreglass insulation to create a thermal chamber, this setup is shown in Figure 4.8 and 4.9.

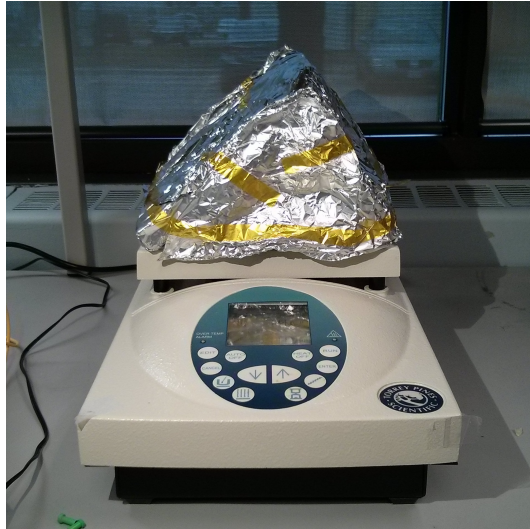The tensile equipment is setup is outlined in Figures 4.10 and 4.11.

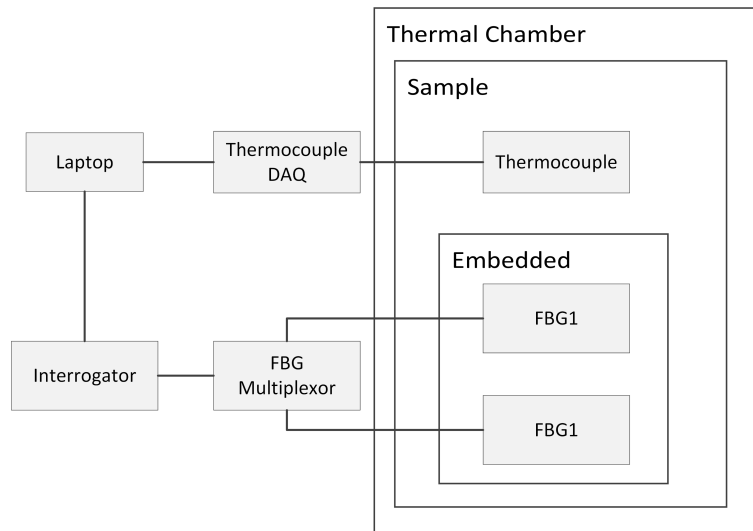Figure 4.8: Thermal chamber for dual parameter sensor temperature testing.

Figure 4.9: Experimental outline for dual parameter sensor temperature testing.
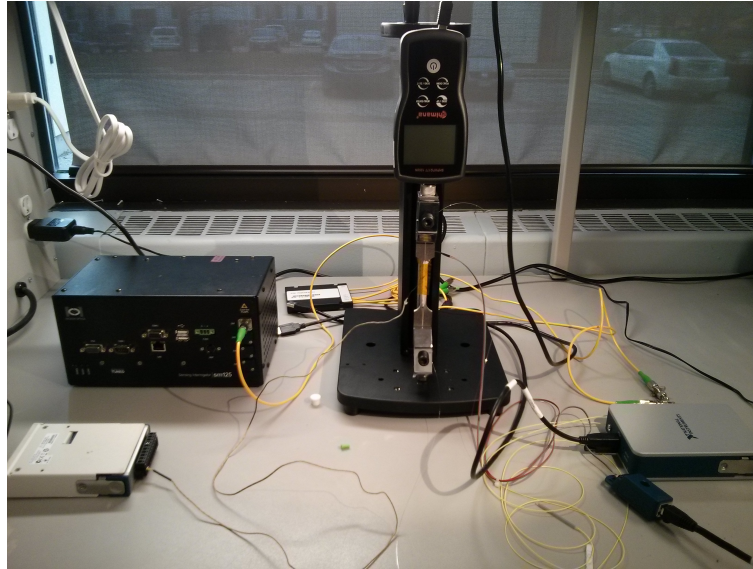
Figure 4.10: Dual parameter sensor temperature testing setup.
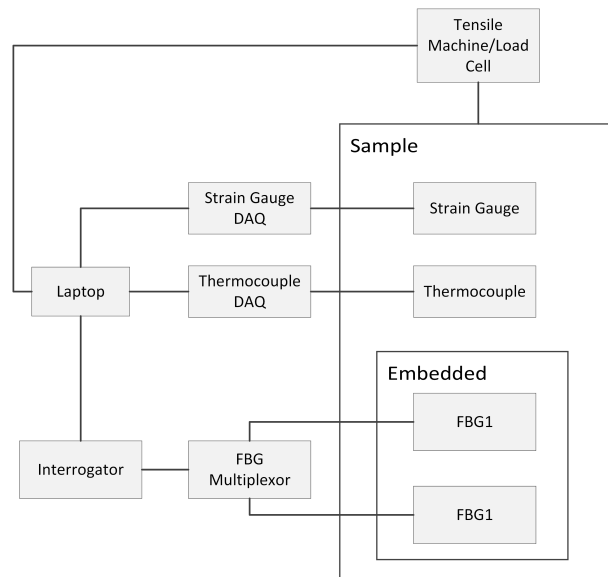
Figure 4.11: Experimental outline for dual parameter sensor tensile testing.

4.2.2 Test Results

Temperature Test

The objective of the temperature test was to observe the behaviour of the two Bragg wavelengths as the temperature of the sample was increased. Figure 4.12a shows the temperature profile of the test. Three step increases were done over a period of 30 minutes. The temperature of the sample along with both Bragg wavelengths were recorded at a rate of 1 Hz. Figure 4.12b shows the recorded Bragg wavelength shift with respect to the recorded temperature during the dual parameter temperature test. Both Bragg wavelengths had a very linear relation to the recorded temperature of the samples. The R^2 of the least squared linear fit for the recorded Bragg wavelengths was 0.9999 and 0.9988.

The most critical result from this test is the sensitivity of the FBGs to the recorded temperature. The expected temperature sensitivity of two FBGs in the dual parameter sample was determined in Section 3.3.3 and can be found in Table 3.6. Table 4.2 shows a comparison of the expected and the recorded temperature sensitivity of both FBGs in the dual parameter sensor. The error for the strain sensitive FBG was 1.4% and the error for the temperature sensitivity FBG was 9.4%.

Table 4.2: Expected and recorded temperature sensitivity of dual parameter sensor.

	Expected Sensitivity	Recorded Sensitivity	Error
Embedded FBG	42.7 pm/°C	42.1pm/°C	1.4%
Floating FBG	11.7 pm/°C	10.6pm/°C	9.4%

The linearity of both Bragg wavelength signals along with the agreement between the analytical model and the experimental results give confidence to the validity of the simpli-
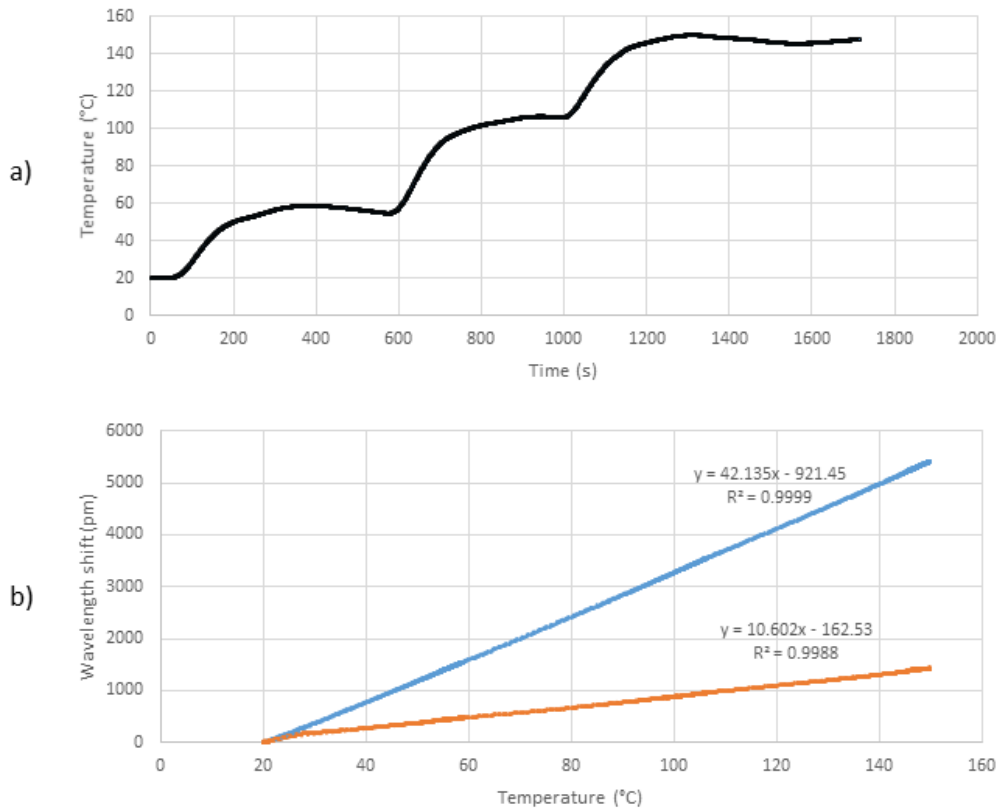
Figure 4.12: a) Temperature profile and b) Bragg wavelength shift for dual parameter temperature test.

fied optomechanical model used in this thesis.

It is also important to note that this temperature test validates the temperature sensitivity of both FBGs but it also implicitly validates the strain sensitivity of the of the FBGs. In Equations 3.3 and 3.5, the simplified optomechanical model shows that the thermo-optic coefficient (ϕ) is a function of the strain-optic coefficient (γ) due to the coupling of temperature and strain by thermal expansion effects. Therefore by confirming that the ϕ model is valid, the γ model must also be valid.

4.2.3 Tensile Test

The objective of the tensile test was to observe the behaviour of the two Bragg wavelengths as the strain of the sample was increased. The strain was increased from 0 to $300\mu\epsilon$ over a period of 250 seconds. The strain vs time plot of the tensile test is shown in Figure 4.13a. The resulting Bragg wavelengths of the two FBGs relative to the reference strain from the strain gauge are shown in Figure 4.13b.
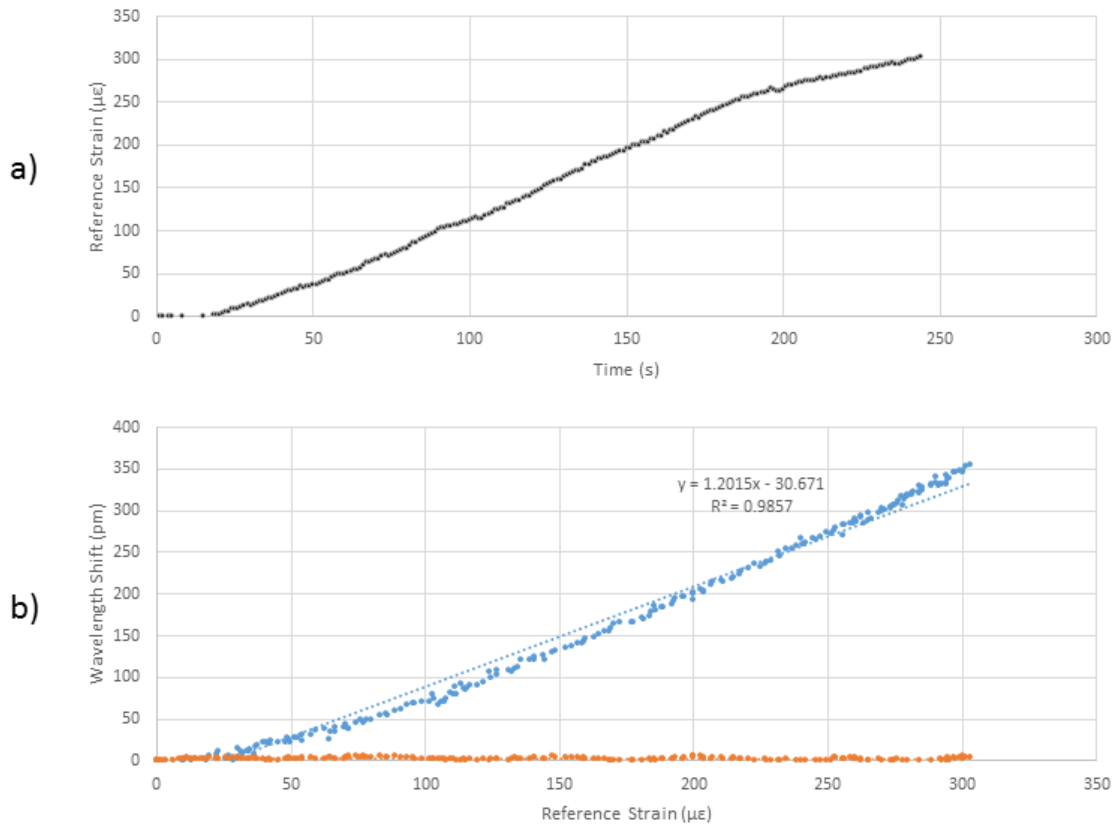
Figure 4.13: a) Strain vs time and b) Bragg wavelength shift for dual parameter strain test.

The two FBGs clearly have different strain sensitivities. The slopes of the wavelength-strain plot in Figure 4.13b are 1.20 and 0 pm/$\mu\epsilon$ for the embedded and floating FBGs

respectively. The strain sensitivities for both FBGs in the floating EDPS were determined analytically in Section 3.3.3. Table 4.3 shows both the recorded strain sensitivity from the tensile test and the expected strain sensitivity from Table 3.6.

Table 4.3: Expected and recorded strain sensitivity of dual parameter sensor.

	Expected Sensitivity	Recorded Sensitivity	Error
Embedded FBG	1.19 pm/$\mu\epsilon$	1.20 pm/$\mu\epsilon$	0.8%
Floating FBG	0 pm/$\mu\epsilon$	0 pm/$\mu\epsilon$	<0.1%

The error between the expected sensitivity and the recorded sensitivity is less than 1% for both the embedded and the floating FBG. The slope for the embedded FBG does have an R^2 value of 0.986 and non-linearity can be seen in Figure 4.13b. The minor non-linearity may have been caused by some bending stress in the sample due to uneven calmping forces.

4.3   Summary of Results

The main goal for all experimental work done in this chapter was validation of the embedding procedure and sensor design. The novel silver nanoparticle embedding process was used to construct both single and dual-parameter sensors. These sensors were subsequently tested and the results were examined.

Seventeen embedded single-parameter sensors were constructed for tensile testing. These sensors were loaded in tension until failure at temperatures ranging from 25°C to 350°C. All sensors successfully recorded strain up until the mean failure strain of 1.6% at 25°C and 0.93% at 350°C. The sensitivity and the linearity of the single parameter sensors seem to confirm the predictions made my the optomechanical models developed in Chapter 3,

77

but due to significant noise in the reference strain and temperature, few conclusive results can be drawn.

Five embedded single-parameter sensors were constructed for repeatability testing. These sensors were put under successive strain and temperature cycles while their output was recorded. The strain varied between 0 and 0.1% while the temperature varied between 0 and 350°C. The temperature and strain sensitivity seemed to be stable during repeated temperature and strain cycles, however, similar noise in the reference strain and temperature signals were seen during the single-parameter tensile tests. More tests with better reference sensors are required to obtain the precision, accuracy, and repeatability values for the single parameter sensors.

A single prototype of an embedded dual-parameter sensor was constructed. The dual parameter sensor was subject to a temperature tests and a tensile test. The sensitivities of both FBGs in the dual-parameter sensor was determined from these tests and compared to the sensitivities predicted by analytical and numerical models described in Chapter 3. The signals from the dual-parameter sensor were linear and the average error between the sensitivities predicted by the models and the measured sensitivities was 2.9%.

Although few tests were done and noisy reference signals reduce the confidence of the obtained results, none of the tests uncovered any catastrophic problems associated with either the embedding process or the design of the sensors. The silver nanoparticle embedding process along with both single and dual-parameter sensor designs have therefore been demonstrated to be viable technologies.

Chapter 5

Conclusions and Future Work

5.1 Conclusions

From this thesis, the following conclusions can be drawn:

1. The use of silver nanoparticle ink as a bulk adhesive has advantages and drawback. The main advantage is the temperature resistance of sintered silver. Silver can sustain much higher temperatures than other polymeric adhesives. Additionally silver nanoparticle paste can be sintered at relatively low temperatures with inexpensive equipment. The main drawback for using silver nanoparticle paste is the shrinkage. Silver nanoparticle paste shrinks significantly during the drying phase and the sintering phase. There are several steps that were taken to avoid the cracking issue. All channels were made as small as possible to minimize the volume of silver required to fill gaps. All surfaces were ultrasonically cleaned and pre-coated with a thin layer of silver ink. The sintering procedure was carefully designed to allow the volatile compounds enough time to evaporate without boiling. The combination of these steps

taken allowed the silver nanoparticle paste to produce an acceptable bond for sensing purposes. Even with the cracking issues, the silver embedding method definitely shows promise when compared to existing FBG embedding methods.

2. Using the mechanical properties of the silver adhesive and optical properties of the fiber, optomechanical models were developed to help predict the behaviour of embedded FBGs. Using these models the critical design criterion for embedded single-parameter sensors was found to be the length of the embedded plain fiber on either side of the grating. If this length was greater than 2.5mm on either side of the grating, perfect strain matching between the fiber and the host material was expected. All other design criteria were secondary to this required length.

3. Using the mechanical properties of the silver adhesive and optical properties of the fiber, optomechanical models were developed to help predict the behaviour of embedded FBGs. Using these models the critical design criterion for embedded single-parameter sensors was found to be the length of the embedded plain fiber on either side of the grating. If this length was greater than 2.5mm on either side of the grating, perfect strain matching between the fiber and the host material was expected. All other design criteria were secondary to this required length.

4. The optomechanical modelling done in this thesis revealed that thermal expansion of the host material causes significant strain on the fiber. Improving the maximum allowable strain on the fiber or using host materials with small coefficients of thermal expansion would significantly improve the overall performance of the embedded sensors.

5. Several design iterations for embedded dual-parameter sensors were completed. A functional prototype of an embedded dual-parameter sensor was created and tested.

During the design process, several critical design criteria for were identified. All gratings should be subject to a uniform strain, strain gradients should be avoided at all costs. Fibers should never be subject to compressive stresses if they are not supported laterally, buckling and fiber failure will occur otherwise. These two design criteria were found to be the most important.

6. Both single-parameter and dual-parameter sensors were constructed and tested. During all single-parameter tests, both the reference temperature and strain signals were excessively noisy. This limited the conclusions that could be drawn from the single parameter tests. Even with noisy reference signals, the single and dual parameter tests showed that the sensors can sustain between 1% to 1.5% strain on average up to at least 350°C.

5.2   Future Work

There are several different subjects in thesis thesis that would require future work.

The embedding procedure developed in this thesis can produce acceptable results, however, the procedure is by no means optimized. The sintering schedule should be optimize to further limit shrinkage and cracking and produce better bonding. Additionally, the examination of different surface coatings on the fiber prior to embedding with silver nanoparticle paste can be examined to improve fiber bond strength and to increase the maximum strain of the fiber.

All tests in this thesis establish a baseline for the performance of FBG sensors embedded with silver nanoparticle paste. The tests performed are not sufficient to fully characterize the performance of this embedding method. Proper reference temperature and strain

sensors should be used along with a more rigorous testing procedure would be needed to characterize accuracy, precision, repeatability, and durability of the sensors with high confidence. Additionally testing related to long term performance and creep should be done.

References

[1] F. Ansari R.M. Measures. *Applications of Fiber Optic Sensors in Engineering Mechanics.* American Society of Civil Engineering, New York, USA, 1993.

[2] C R Liao and D N Wang. Photonic Sensors Review of Femtosecond Laser Fabricated Fiber Bragg Gratings for High Temperature Sensing . *Photonic Sensors*, 3(2):97–101, 2013.

[3] Manfred Kreuzer. Strain measurement with fiber bragg grating sensors. *HBM, Darmstadt, S2338-1.0 e*, 2006.

[4] H N Li, L Ren, D S Li, and T H Yi. Design and applications of fiber Bragg grating sensors for structural health monitoring. In *Advances in Structural Engineering and Mechanics (ASEM13)*, pages 2215–2221, 2013.

[5] Christopher K Y Leung, Kai Tai Wan, Daniele Inaudi, Xiaoyi Bao, Wolfgang Habel, Zhi Zhou, Jinping Ou, Masoud Ghandehari, Hwai Chung Wu, and Michio Imai. Review: optical fiber sensors for civil engineering applications. *Materials and Structures*, 48(4):871–906, 2015.

[6] Wenjuan Wang, Hao Song, Jingfeng Xue, Wei Guo, and Minghui Zheng. Overview of intelligent composites with embedded FBG sensors. *Proceedings of the 2011 IEEE 5th International Conference on Cybernetics and Intelligent Systems, CIS 2011*, pages 47–51, 2011.

[7] Liqun Tang, Xiaoming Tao, and Chung-loong Choy. Effectiveness and optimization of fiber Bragg grating sensor as embedded strain sensor. *Smart Materials and Structures*, 8(1):154–160, feb 1999.

[8] Margit Harsch, József Karger-Kocsis, and Florian Herzog. Monitoring of cure-induced strain of an epoxy resin by fiber Bragg grating sensor. *Journal of Applied Polymer Science*, 107(2):719–725, jan 2008.

83

[9] Nouari Saheb and Samir Mekid. Fiber-embedded metallic materials: From sensing towards nervous behavior. *Materials*, 8(11):7938–7961, 2015.

[10] Ralf D Pechstedt, Harwell Science, and Innovation Campus. Fiber optical sensors for aircraft applications. 9226(0):1–11, 2014.

[11] Mustafa Kemal Kulekci. Magnesium and its alloys applications in automotive industry. *International Journal of Advanced Manufacturing Technology*, 39(9-10):851–865, 2008.

[12] Ronghui Qua Zujie Fang, Ken Chin and Haiwen Cai. *Fundamentals of Optical Fiber Sensors*. Wiley, Hoboken, USA, 2012.

[13] Z. Zhu, Y. Chen, and Y. Zhang. The temperature sensitivity of fiber bragg gratings embedded in an Al 6061 matrix by ultrasonic welding. *Journal of Intelligent Material Systems and Structures*, 22(18):2173–2179, 2011.

[14] R R J Maier, D Havermann, O Schneller, J Mathew, D Polyzos, W. N. MacPherson, and D P Hand. Optical fibre sensing in metals by embedment in 3D printed metallic structures. *Proc. SPIE 9157, 23rd International Conference on Optical Fiber Sensors*, 9157:1–4, 2014.

[15] Hamidreza Alemohammad and Ehsan Toyserkani. Metal Embedded Optical Fiber Sensors: Laser-Based Layered Manufacturing Procedures. *Journal of Manufacturing Science and Engineering*, 133(June 2011):031015, 2011.

[16] Carlo Massaroni, Paola Saccomandi, and Emiliano Schena. Medical smart textiles based on fiber optic technology: An overview. *Journal of Functional Biomaterials*, 6(2):204–221, 2015.

[17] Xu Dong Wang and Otto S. Wolfbeis. Fiber-Optic Chemical Sensors and Biosensors (2013-2015). *Analytical Chemistry*, 88(1):203–227, 2016.

[18] Sakurambo. Fiber bragg grating image, with removed refractive indices. https://en.wikipedia.org/wiki/Fiber_Bragg_grating. Accessed: 2016-12-20, CC-SA-3.0 GFDL.

[19] Fang Xie, Xianfeng Chen, Lin Zhang, and Ming Song. Realisation of an effective dual-parameter sensor employing a single fibre Bragg grating structure. *Optics and Lasers in Engineering*, 44(10):1088–1095, 2006.

[20] Xiuping Liu, Tingting Wang, Yu Wu, Yuan Gong, and Yun Jiang Rao. Dual-parameter sensor based on tapered FBG combined with microfiber cavity. *IEEE Photonics Technology Letters*, 26(8):817–820, 2014.

[21] H R Alemohammad, E Foroozmehr, B S Cotten, and E Toyserkani. A dual-parameter optical fiber sensor for concurrent strain and temperature measurement: Design, fabrication, packaging, and calibration. *Journal of Lightwave Technology*, 31(8):1198–1204, 2013.

[22] Tian You and Richard Liang. Dual-Parameter Opto-Mechanical Fiber Optic Sensors for Harsh Environment Sensing : Design , Packaging , Calibration , and Applications by. 2014.

[23] Klas Weman. *Welding processes handbook. [electronic resource].* 2012.

[24] C. Zhang L. Li. *ASM Handbook*, volume 6A. ASM International, 2011.

[25] Fabrisonic. http://fabrisonic.com/. Accessed: 2016-11-21.

[26] Dezhi Li and Rupert C. Soar. Plastic flow and work hardening of Al alloy matrices during ultrasonic consolidation fibre embedding process. *Materials Science and Engineering A*, 498(1-2):421–429, 2008.

[27] Dezhi Li and Rupert C. Soar. Characterization of process for embedding SiC fibers in Al 6061 O matrix through ultrasonic consolidation. *Journal of Engineering Materials and Technology*, 131(2):021016, 2009.

[28] Yulong Li, Wen Liu, Yan Feng, and Hua Zhang. Ultrasonic embedding of nickel-coated fiber Bragg grating in aluminum and associated sensing characteristics. *Optical Fiber Technology*, 18(1):7–13, 2012.

[29] Y. C. Chen, D. Bakavos, A. Gholinia, and P. B. Prangnell. HAZ development and accelerated post-weld natural ageing in ultrasonic spot welding aluminium 6111-T4 automotive sheet. *Acta Materialia*, 60(6-7):2816–2828, 2012.

[30] Jeganathan Karthikeyan. Cold Spray Process. *Thermal Spray Technology*, 5:77–84, 2013.

[31] Dirk Havermann, Jinesh Mathew, William N. MacPherson, Robert R. J. Maier, and Duncan P. Hand. Temperature and Strain Measurements with Fibre Bragg Gratings Embedded in Stainless Steel 316. *Journal of Lightwave Technology*, 33(12):1–1, 2014.

[32] Albert J Osei and Joseph Grant. Investigation of Structural Properties of Carbon-Epoxy Composites. pages 1–5, 2002.

[33] Chia-chin Chiang. Curing Monitoring of Composite Material Using Embedded Fiber Bragg Grating Sensors. 2007.

[34] M. Harsch, J. Karger-Kocsis, and F. Herzog. Strain development in a filled epoxy resin curing under constrained and unconstrained conditions as assessed by Fibre Bragg Grating sensors. *Express Polymer Letters*, 1(4):226–231, 2007.

[35] T. Grandal, E. Piñeiro, A. Asensio, and F. Rodriguez. Metallic coating techniques for fiber Bragg grating sensors. 8785:878538, 2013.

[36] Debdatta Ratna. General Introduction to Thermoset Networks 1.1. In *Handbook of thermoset resins*, pages 1–59. 2009.

[37] Aremco high temperature epoxies. http://www.aremco.com/high-performance-epoxies/. Accessed: 2016-11-24.

[38] Farhad Ansari and Yuan Libo. Mechanics of Bond and Interface Shear Transfer in Optical Fiber Sensors. *Journal of Engineering Mechanics*, 124(4):385–394, 1998.

[39] Huaping Wang and Zhi Zhou. Advances of strain transfer analysis of optical fibre sensors. *Pacific Science Review*, 16(1):8–18, 2014.

[40] Hang-Yin Ling, Kin-Tak Lau, Wei Jin, and Kok-Cheung Chan. Characterization of dynamic strain measurement using reflection spectrum from a fiber Bragg grating. *Optics Communications*, 270(1):25–30, 2007.

[41] Yue Qiu and Yunlong Sheng. Fiber Bragg Grating Modeling. *Center for Optics, Photonics and Lasers, Laval University.*

[42] K. S C Kuang, R. Kenny, M. P. Whelan, W. J. Cantwell, and P. R. Chalker. Embedded fibre Bragg grating sensors in advanced composite materials. *Composites Science and Technology*, 61(10):1379–1387, 2001.

[43] I.H. Malitson. Interspecimen Comparison of the Refractive Index of Fused Silica. 55(10), 1965.

[44] Novacentrix metalon conductive inks. http://www.novacentrix.com/products/metalon-inks. Accessed: 2016-10-18.

[45] Tao Wang, Meihua Zhao, Xu Chen, Guo Quan Lu, Khai Ngo, and Shufang Luo. Shrinkage and sintering behavior of a low-temperature sinterable nanosilver die-attach paste. *Journal of Electronic Materials*, 41(9):2543–2552, 2012.

[46] Kim S. Siow. Mechanical properties of nano-silver joints as die attach materials. *Journal of Alloys and Compounds*, 514:6–19, 2012.

[47] Nanotach (nanosilver paste): X series. http://www.nbetech.com/products.shtml. Accessed: 2016-10-14.

[48] *Engineered Materials Handbook Desk Edition.* ASM International, 1995.

[49] J.F. Lancaster. *Metallurgy of Welding.* Woodhead Publishing Limited, Cambridge, England, 1999.

[50] A.A. Nayeb-Hashemi and J. B. Clark. The Ag-Mg (Silver-Magnesium) System 107.8682 24.305. 5(4):348–358, 1984.

[51] Yiyu Wang, Guoqiang Luo, Leijun Li, Qiang Shen, and Lianmeng Zhang. Formation of intermetallic compounds in Mg-Ag-Al joints during diffusion bonding. *Journal of Materials Science*, 49(20):7298–7308, 2014.

[52] Micron optics static optical sensing interrogator — sm125. http://www.micronoptics.com/product/static-optical-sensing-interrogator-sm125/. Accessed: 2016-10-18.

[53] M. John Matthewson, Charles R. Kurkjian, and Jesse R. Hamblin. Acid stripping of fused silica optical fibers without strength degradation. *Journal of Lightwave Technology*, 15(3):490–497, 1997.

[54] Frederick T. Wallenberger, James C. Watson, and Li Hong. Glass Fibers. *ASM Hanbook*, 21(Ref 19):27–34, 2001.

APPENDICES

Appendix A

Matlab Implementation of Optomechanical Model of FBG with Non-Uniform Strain Distribution

```
1  %————————————————————————————————————————
2  %spectrum calculation function
3  %————————————————————————————————————————
4  %This function calculates the spectral response
5  %of an FBG under a user defined strain distribution.
6  %This function takes in optical parameters and strain parameters and
7  %can be used for design optimization. It is very time efficient.
8  %
9  %input parameters:
10 %strainDistribution − this is the strain distribution along the length
11 %of the FBG. It should be a vertical nx1 matrix variable containing
12 %nondimensional strain values (not percent)
13 %
14 %output parameters:
15 %none (the function will automatically plot the resulting spectrum)
16 %
17 %
18 %Based on: "Characterization of dynamic strain measurement using
19 %reflection spectrum from a fiber Bragg grating" − Hang−Yin Ling,
       2007,
20 %optics communication
```

```matlab
21  %
22  %Author: Philippe Meszaros
23  %email: pmeszaro@uwaterloo.ca
24  %—————————————————————————————
25  function saved1=spectrumFuncThesis(strainDistribution)
26
27  %FBG optical parameters
28  L=1e-3;                    %FBG length (m)
29  lambda_0=1530E-9;          %strain free wavelength (m)
30  v=1;                       %fringe visibility
31  n_eff0=1.44;               %refractive index of core
32  dn_eff_bar=1e-4;           %DC index change
33
34
35  %Strain optic parameter
36  pe=0.22;
37
38  %initialize spectrum range for analysis (You can change this)
39  lambda_min=1524e-9;        %lower bound
40  lambda_max=1550e-9;        %upper bound
41  d_lambda=0.01e-9;          %resolution (lower resolution=faster)
42
43  %initialize wavelength and reflectance output vectors
44  X=zeros(1,(lambda_min-lambda_max)/d_lambda);    %(wavelength)
45  Y=X;                                            %(reflectance)
46
47  %strain data
48  M=length(strainDistribution); %number of divisions of constant strain
49  e=strainDistribution ';
50  dz=L/M;
51
52  %Strain effects
53  lambda_b=lambda_0*(1+(1-pe)*e);   %strain wavelength vector
54
55  %—————————————————————————————
56  %note that these calculated values are in matrices spanning
57  %the length of the FBG and the range of frequencies being analyzed
58  %(very dirty but efficient, do not touch unless absolutely necessary)
59  lambda=lambda_min:d_lambda:lambda_max;
60  lambda=lambda '; %wavelength variable vector
```

```matlab
61
62  %AC coupling coefficient
63  k=pi./lambda*v*dn_eff_bar;
64  k=repmat(k,1,length(lambda_b));
65
66  %DC coupling coefficient
67  sigma_del= 2*pi*n_eff0.*(repmat(lambda, 1, length(lambda_b)).^(-1)-...
68      repmat(lambda_b, length(lambda), 1).^(-1))...
69      +2*pi./repmat(lambda, 1, length(lambda_b)).*...
70      repmat(dn_eff_bar, length(lambda), length(lambda_b));
71
72  gamma_b=(k.^2-sigma_del.^2).^(1/2);
73
74  %calculate elements of F
75  F11=cosh(gamma_b*dz)-1i*sigma_del./gamma_b.*sinh(gamma_b*dz);
76  F21= -1i*k./gamma_b.*sinh(gamma_b*dz);
77  F12= 1i*k./gamma_b.*sinh(gamma_b*dz);
78  F22=cosh(gamma_b*dz)+1i*sigma_del./gamma_b.*sinh(gamma_b*dz);
79
80  %calculate reflectivity for all wavelengths
81  for ii=1:length(lambda)
82
83      %Find F————————————————
84      F=eye(2);
85      %spanning the length of the fiber
86      for jj=1:M
87          F=[F11(ii,jj),F21(ii,jj);F12(ii,jj),F22(ii,jj)]*F;
88      end
89      %————————————————————————
90
91      %solve for back propagating mode at start of FBG
92      R=1/F(1, 1);
93      S=R*F(2, 1);
94      reflec=abs(S/1)^2;
95
96      %save result
97      X(index)= lambda(ii);
98      Y(index)= reflec;
99
100     index=index+1;
```

```matlab
101
102    end
103
104    %plot data (comment out if unnecessary)
105    hold on;
106    Y_db=10*log10(Y);
107
108    %add noise floor from interrogator at −40db
109    for i=1:length(Y_db)
110        if Y_db(i) <=−40
111            Y_db(i)=−40 + rand() −0.5;
112        end
113    end
114
115    plot(X.*10^9, Y_db);
116
117    xlabel('Wavelength (nm)');
118    ylabel('Reflected Power (dB)');
119    drawnow;
120    end
```
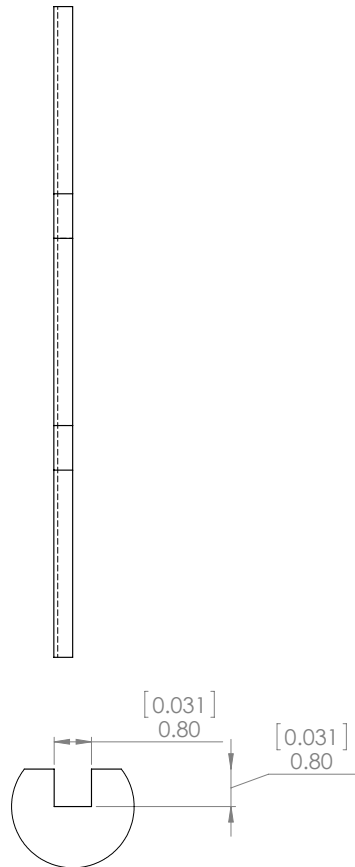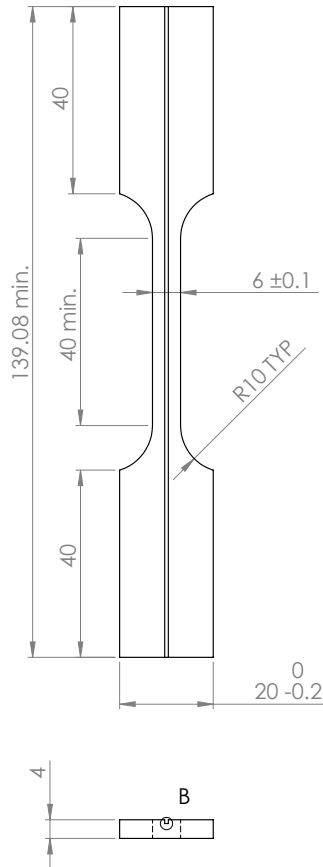
Appendix B

Tensile Test Sample Drawings

40

139.08 min.

40 min.

40

6 ±0.1

R10 TYP

0
20 -0.2

4

A

[0.008]
0.20

[0.008]
0.20
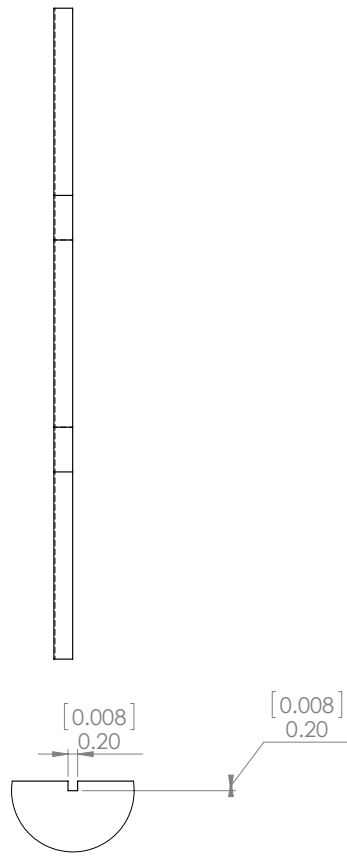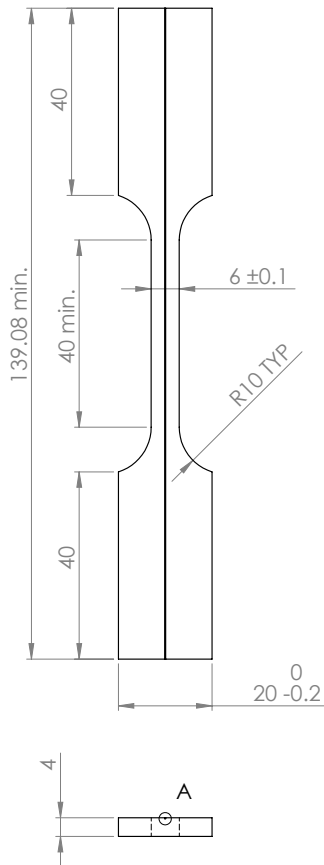
DETAIL A
SCALE 10 : 1

Quantity: 35 pieces
Note: Use slitting saw (McMaster-Carr P/N: 3044A38 with 1/2" arbor)

UNLESS OTHERWISE SPECIFIED: DIMENSIONS ARE IN MM SURFACE FINISH: TOLERANCES: LINEAR: +/- 1MM ANGULAR:		FINISH:				DEBUR AND BREAK SHARP EDGES	DO NOT SCALE DRAWING		REVISION	B
							Univeristy of Waterloo			
	NAME	SIGNATURE	DATE				TITLE:			
DRAWN	R. Liang		16/02/02				Single Parameter Sample			
CHK'D										
APPV'D										
MFG										
Q.A				MATERIAL:			DWG NO.			A4
				WEIGHT:			SCALE:1:1		SHEET 1 OF 2	

40

139.08 min.

40 min.

6 ±0.1

R10 TYP

40

0
20 -0.2

4

B

[0.031]
0.80

[0.031]
0.80

DETAIL B
SCALE 10 : 1

Quantity: 10 pieces

UNLESS OTHERWISE SPECIFIED: DIMENSIONS ARE IN MM SURFACE FINISH: TOLERANCES: LINEAR: +/- 1MM ANGULAR:		FINISH:			DEBUR AND BREAK SHARP EDGES		DO NOT SCALE DRAWING		REVISION	B
	NAME	SIGNATURE	DATE				**Univeristy of Waterloo**			
DRAWN	R. Liang		16/02/02				TITLE:			
CHK'D							**Dual Parameter Sample**			
APPV'D										
MFG										
Q.A				MATERIAL:			DWG NO.			A4
			WEIGHT:			SCALE:1:1		SHEET 2 OF 2	

95